Model for the Gas Evolution in a Porous Medium Driven by Solute Diffusion

Ioannis N. Tsimpanogiannis and Yannis C. Yortsos
Dept. of Chemical Engineering, University of Southern California, Los Angeles, CA 90089

An effective continuum model is derived to describe the nucleation and subsequent growth of a gas phase from a supersaturated, slightly compressible binary liquid in a porous medium, driven by solute diffusion. The evolution of the gas results from reducing the system pressure at a constant rate or withdrawing the liquid at a constant rate. The model addresses two stages before the onset of bulk gas flow, nucleation and gas-phase growth. Negligible gradients due to gravity or viscous forces are assumed, so the critical gas saturation signaling the onset of bulk gas flow is only a function of the nucleation fraction. Important quantities characterizing the process, such as the pore number fraction hosting activated sites, deviation from thermodynamic equilibrium, maximum supersaturation, and critical gas saturation, depend crucially on the nucleation characteristics of the medium. Heterogeneous nucleation models using preexisting gas trapped in hydrophobic cavities or in terms of a rate-dependent nucleation are used to investigate the nucleation behavior. Using a simpler analytical model the relevant quantities during nucleation can be expressed in terms of a simple combination of dimensionless parameters. The theory predicts that the maximum supersaturation is a weakly increasing function of rate, which in the region of typical experimental parameters can be approximated as a power law. It depends sensitively on the probability density function of nucleation cavity sizes. The final nucleation fraction (thus, the critical gas saturation) is predicted to be a power law of the decline rate. The theoretical exponents agree well with experimental data. The subsequent evolution of the gas phase and the approach to the critical gas saturation is also described.

Introduction

The liquid-to-gas phase change in a porous medium and the subsequent growth of the gas phase are encountered in many applications driven by mass or heat transfer. These span various fields of scientific interest and a range of length scales. Examples include the solution gas-drive process for the recovery of oil from oil reservoirs (Sheng et al., 1999a,b), boiling in porous media (Thome, 1990; Satik and Yortsos, 1996), thermal methods for oil recovery (Prats, 1982), nuclear-waste disposal (Doughty and Pruess, 1990), and soil remediation (Ho and Udell, 1995). In this article, we focus on the isothermal gas-phase growth from a supersaturated, slightly compressible, binary liquid in a porous medium. This is driven by mass transfer, the extent of which is controlled by the application of either a constant-rate decline of the system pressure or the withdrawal of the liquid at a constant rate.

Consider the removal of an initially supersaturated liquid from a porous medium of a fixed volume (Figure 1). As the pressure continuously declines, due to liquid expansion, the bubble point of the liquid is eventually reached. Then, nucleation of a gas phase starts, at rates depending on the nucleation properties of the medium. Nucleation is manifested either in the release of preexisting gas bubbles, trapped in hydrophobic cavities, or in the form of heterogeneously nucleated nuclei. Emphasis will be placed on the former mechanism, although the conventional model will also be used. Because of the competing processes of bubble growth, which depletes the solute from the liquid, thus, reducing the super-

---

Correspondence concerning this article should be addressed to I. N. Tsimpanogiannis.

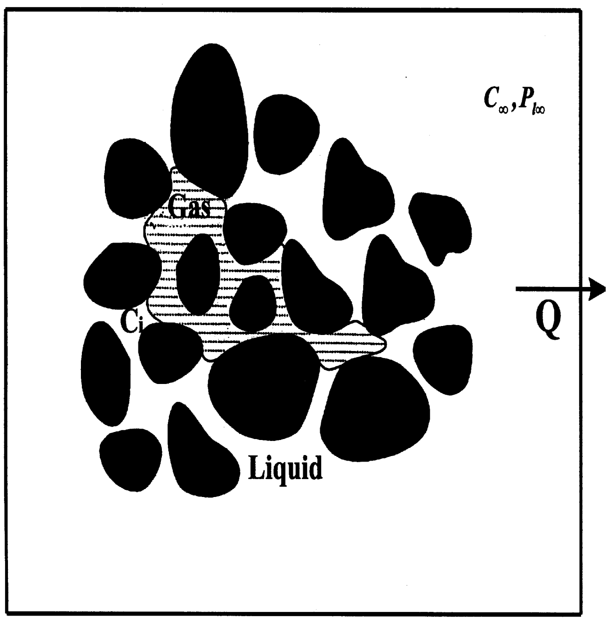

Figure 1. Gas cluster growth in a porous medium, driven by the decline of pressure at constant rate.

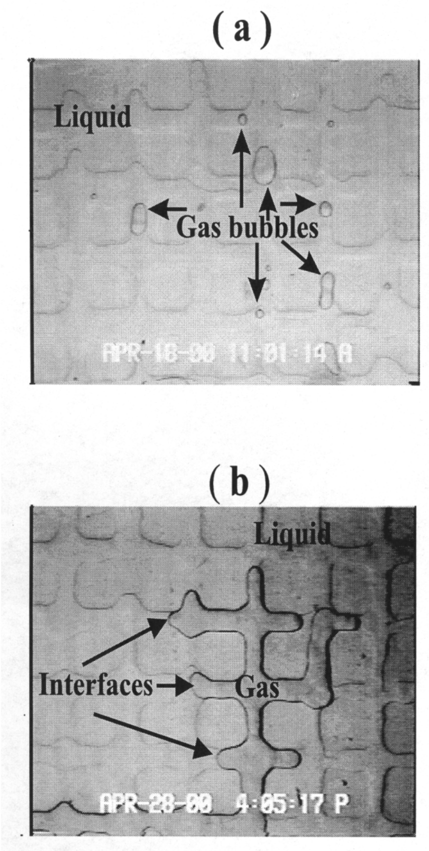

Figure 2. Micromodel snapshots indicating (a) gas bubbles confined within single pore throats/bodies; (b) gas bubble spanning several pore bodies.

saturation, and the liquid withdrawal, which reduces the pressure, thus, increasing the supersaturation, a supersaturation maximum is attained, following which nucleation terminates. Identifying the maximum supersaturation and its dependence on process parameters is a key issue. The subsequent gas evolution is controlled by the available supersaturation, the solute mass transfer from the liquid to the gas, and the capillary characteristics of the porous medium. The gas phase appears first in the form of small bubbles growing within the confines of single pores (Figure 2a), but ultimately takes the form of large clusters, spanning a number of pores (Figure 2b). Competition for mass transfer between the growing bubbles or clusters, capillary effects at pore constrictions, viscous and gravity forces, and the possibility of coalescence or the snap-off of gas-liquid interfaces are important factors in determining the gas-phase evolution.

Eventually, gas flows as a bulk phase. The onset of flow is signaled when the gas pore-volume fraction, S_g, becomes equal to the so-called critical gas saturation, S_{gc}, a value that depends on the underlying growth and flow mechanisms. If viscous or gravity gradients are negligible, gas flow occurs for the first time when isolated gas clusters connect to form a sample-spanning (percolation) cluster (Yortsos and Parlar, 1989). If they do not, gas flow and production occur through the continuous motion of finite-size gas clusters, subject to various mechanisms of interaction, including coalescence. This simultaneous flow of gas and liquid is quite complex, particularly under strong pressure gradients, for example, in the case of high-viscosity oils, where "foamy" oil flow takes place (Smith, 1988; Maini, 1996, 1999). In this article, we will only consider the stage before the onset of gas flow, however, and in the absence of significant gravity or viscous gradients.

A number of studies on this problem have been reported. A review of the early literature can be found in Li and Yortsos (1995a,b). Experimental work for the case of constant pressure decline rate in consolidated porous media using light oils was reported by Moulu and Longeron (1989), Moulu (1989), and Scherpenisse et al. (1994). Sheng et al. (1999b), Wong et al. (1999), and Urgelli et al. (1999) conducted experiments with heavy oils. Visualization experiments with light oils were reported by Li and Yortsos (1995a), Hawes et al. (1997), Mackay et al. (1998), and Dominguez et al. (2000). Bora et al. (2000) reported experiments with heavy oils. These studies have shown that the critical gas saturation is an increasing function of the liquid withdrawal rate, a finding explained by the increasing number of nucleation centers at larger depletion rates. Scherpenisse et al. (1994) provided useful, but qualitative, scaling arguments showing that maximum supersaturation and critical gas saturation are power-law functions of the depletion rate. A theoretical analysis of bubble growth by solute diffusion in which mass transfer and porous medium capillarity dominate, was provided by Li and Yortsos (1995a,b). The authors conducted visualization experiments in glass micromodels and pore-network simulations to explain patterns and rates of growth of the gas phase at the pore-network scale. Along similar lines, Du and Yortsos (1999) provided a pore-network analysis of the critical gas saturation in the absence of gravity/viscous gradients. They confirmed an earlier hypothesis by Yortsos and Parlar (1989) that in the absence of spatial gradients, the onset of critical gas saturation coincides with the percolation threshold of an invasion percolation process, originating from multiple nucleation centers. They also showed that S_{gc} is a power law of the final nucleation fraction (defined more precisely below), f_{qf}, namely

$$S_{gc} = f_{qf}^{1-D_f/E} \tag{1}$$

Here, E (equal to 2 or 3) is the (Euclidean) dimension of the pore network and D_f is the mass fractal dimension of the percolation cluster (equal to 1.82 for 2-D invasion percolation (IP) with trapping, and 2.53 for 3-D IP with or without trapping; Feder, 1988). The dependence in Eq. 1 was established regardless of the nucleation sequence (instantaneous or sequential) or the particular regime of bubble growth (see Li and Yortsos, 1995a,b).

The presence of gradients will affect the preceding scaling. Pore-network simulations conducted by McDougall and Sorbie (1999) and Wang and Mohanty (1999) in the related topic of gas condensation, showed that S_{gc} decreases as the hydrostatic pressure gradient increases, a trend also anticipated in Scherpenisse et al. (1994). In a parallel study (Tsimpanogiannis and Yortsos, 2002), we have analyzed the effect of gravity and/or viscous forces on S_{gc}, and developed scaling laws for the dependence of S_{gc} on f_{qf} and on two dimensionless parameters, the Bond and capillary numbers, defined respectively as

$$B = \frac{\Delta \rho g k}{\gamma} \quad \text{and} \quad Ca = \frac{q \mu}{\gamma} \tag{2}$$

Here $\Delta \rho$ denotes the density difference between liquid and gas, k is permeability, γ the liquid–gas interfacial tension, q the liquid flow rate, and μ the liquid viscosity. Equation 1 is obtained in the limits $B \ll 1$ and $Ca \ll 1$ (more specifically, $B \leq 10^{-3}$ and $Ca \leq 10^{-3}$), which are the regions of interest of this article.

In many practical cases, pressure depletion is due to liquid withdrawal at a constant flow rate. Experimental work in consolidated porous media with light oils was reported by Firoozabadi et al. (1992), Firoozabadi and Aronson (1999), and Egermann and Vizika (2000). These studies focused on the critical gas saturation, which was found to be an increasing function of the liquid withdrawal rate. As before, this finding was explained by the increasing number of nucleation centers, from which gas clusters grow at larger depletion rates. Sheng et al. (1999a) and Renard et al. (2000) in two recent reviews focused on aspects of solution gas drive related to the primary recovery of heavy oil.

A modeling attempt to capture the gas-phase growth, but not the preceding nucleation period, in an experiment at a constant rate of withdrawal, was made by Firoozabadi and Kashchiev (1996). These authors used an effective continuum model with bubble growth driven by diffusion. The gas phase is modeled as a collection of effective bubbles, mass transfer to which is approximated by simple expressions. Although the article discusses rate-dependent nucleation using classical expressions (see also below), the nucleation issues is in fact bypassed, in that nucleation fraction, the maximum supersaturation, or the effect of depletion rate on the number of bubbles nucleated, are not actually predicted or calculated. Rather, the latter quantities are inferred from the experimental results, and subsequently used as parameters for the gas-phase growth following the nucleation period.

Experiments on pressure depletion driven by constant liquid withdrawal rate, particularly with heavy oils, were reported by Pooladi-Darvish and Firoozabadi (1999), Tang and Firoozabadi (1999), Kumar et al. (2000), Andarcia et al. (2001), Arora and Kovscek (2001), and Kamp et al. (2001a,b). In two very recent studies, which appeared at the same time this work was being written, Kamp et al. (2001a) and Arora and Kovscek (2001) presented effective continuum models to interpret the pressure depletion of heavy oils, focusing in particular on the foamy oil issue. Because of the high viscous forces in these experiments, these models must also account for a two-phase flow, which was done using conventional relative permeability functions. In the present context, these studies are of interest insofar as nucleation is concerned. The latter is incorporated in the form of rate-dependent nucleation in Kamp et al. (2001a), and in the form of activated cavities in Arora and Kovscek (2001). Nucleation parameters were estimated to match experimental data (see more discussion below).

The objective of this article is to provide a comprehensive model of both the nucleation and the gas-phase growth periods, until the onset of the critical gas saturation. For this purpose, an effective continuum model will be developed. If used to model the later stages of bubble growth, where gas occupies several pores and is influenced by the pore geometry, topology, and capillarity (for example, see Li and Yortsos, 1995a,b), effective continuum models have obvious drawbacks. However, they may be adequate for describing nucleation and the early stages of bubble growth. The last two, particularly the nucleation sequence, are the main areas of interest of this article. We focus on the effect of the nucleation characteristics on the maximum supersaturation, the nucleation fraction, and the critical gas saturation, and provide an analysis of the effect of various parameters, such as pressure decline rate, on these quantities. Results for the gas-phase growth following the conclusion of nucleation are also presented.

The article is organized as follows: first, we formulate the problem. A scaling analysis allows to recast the problem in a more useful form, to be used for direct predictions. Then, numerical results are analyzed. It turns out that for their interpretation, a simplified model of the nucleation and growth periods can be developed. We use the simpler model to obtain expressions for the maximum supersaturation as a function of geometric, thermodynamic, and process parameters. This allows us to obtain useful relations for the dependence of the final nucleation fraction and the critical gas saturation on process parameters. The theoretical predictions are then compared against experimental results.

Mathematical Formulation

Consider the heterogeneous nucleation and growth of multiple bubbles from a binary liquid within an effective porous medium. The process is driven by the continuous increase in the supersaturation of the system, $KC_\infty(t) - P_l(t)$, where for simplicity we have assumed linear thermodynamic equilibria using Henry's law

$$P_g = KC_\infty(t) \tag{3}$$

Here, K is the solubility constant, $C_\infty(t)$ the time-varying mass concentration, P stands for pressure, and subscripts g and l denote gas and liquid, respectively. More complex thermodynamics can certainly be incorporated, but the salient features are manifested with the simpler model of Eq. 3. As noted earlier, the change in supersaturation can be imposed in two different ways, one in which the pressure declines at a constant rate, and another in which the liquid is withdrawn at a constant rate. Because gravitational and/or viscous effects are not included, the pressure is spatially uniform. Instead, emphasis is placed on nucleation and on the effect of the increase of supersaturation on the growth of the gas phase.

Nucleation

As the liquid pressure declines, nucleation sets in. Yortsos and Parlar (1989) reviewed the gas–liquid phase change in a porous media and concluded that heterogeneous nucleation is the most plausible mechanism in solution gas drives [see also more recent reviews by Laaksonen et al. (1995) and Jones et al. (1999)]. In one model, nucleation occurs when a gas bubble, either preexisting or nucleated inside a cavity at the pore walls, becomes unstable and detaches or otherwise occupies the host pore body (Figure 3). This type of mechanism is in agreement with visual observations from micromodel experiments (Li and Yortsos, 1995a; El Yousfi et al., 1991, 1997; Bora et al., 2000; Dominguez et al., 2000). In the cavity model, the condition for the activation of a nucleation site is when the trapping capillary forces are overcome for the first time (Figure 3). This occurs when the following condition is satisfied between the radius of the nucleation cavity, r_c, and supersaturation

$$\frac{2\gamma \cos\theta}{r_c} = KC_\infty(t) - P_l(t) \tag{4}$$

where θ is the contact angle ($0 < \theta < \pi/2$). In this model, the onset of nucleation is not kinetically related to the degree of supersaturation, as for example, in conventional approaches (Firoozabadi and Kashchiev, 1997), but rather depends on the size distribution, $\alpha_c(r_c)$, of the nucleation cavities.

Now consider the activation of nucleation sites. With the decrease in the liquid pressure, the righthand side of Eq. 4 increases, eventually becoming positive. Then, various cavities satisfying Eq. 4 become activated and their corresponding host pore bodies occupied by gas. At any time, the current nucleation fraction, f_q, defined as the number fraction of pores that contain sizes that have been activated, is

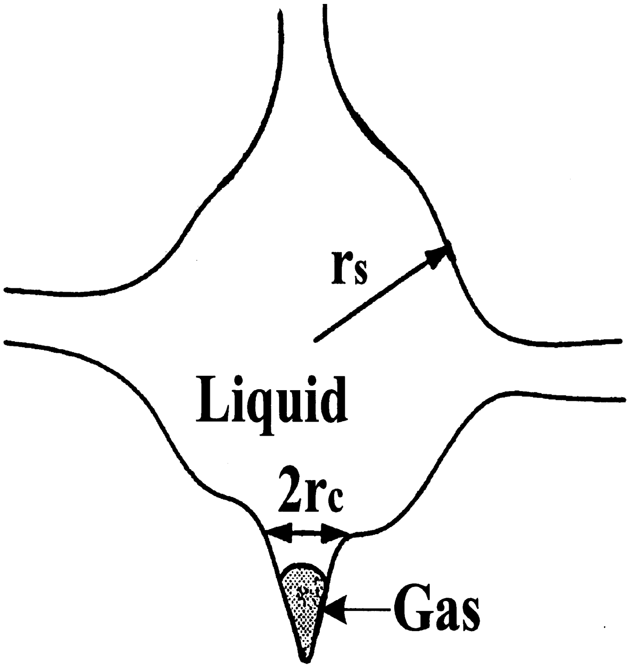

Figure 3. Nucleation cavity in a host pore body.

$$f_q = \int_{r_c}^{\infty} \alpha_c(r)\ dr \tag{5}$$

where r_c is an implicit function of time, through Eq. 4. Equation 5 implies a zero nucleation fraction at zero supersaturation ($r_c \to \infty$) and a nucleation fraction of one at infinite supersaturation ($r_c \to 0$). The cavity-size distribution, α_c, pertains only to the largest cavity in any given pore (as this cavity will be activated first). The actual number of bubbles contained in a given pore may be larger. We will assume that a number of bubbles, n_B, are contained in each activated pore. Parameter n_B will be taken equal to 1 for the cavity model, as this is suggested in the micromodel experiments, but will be kept arbitrary for rate-dependent heterogeneous nucleation. Equation 5 slightly overestimates the true nucleation fraction, since pores containing sites to be activated later may already be occupied by gas, due to the growth of gas clusters from neighboring pores. A more appropriate expression in such a case would be

$$\frac{df_q}{dt} = (1 - S_g)\frac{d}{dt}\left[\int_{r_c}^{\infty} \alpha_c(r)\ dr\right] \tag{6}$$

where S_g is the gas saturation. However, in most cases, nucleation terminates well before gas bubble growth has occurred to any substantial degree ($S_g \ll 1$), thus, Eq. 5 should be an excellent approximation.

It is interesting to illustrate the dependence of f_q on the various cavity-size distributions. For a Rayleigh distribution

$$\alpha_c(r) = \frac{\pi r}{2r_c^{*2}} \exp\left(-\frac{\pi r^2}{4r_c^{*2}}\right) \tag{7}$$

where r_c^* is a characteristic (here the mean) cavity size, Eq. 5 reads

$$f_q = \exp\left(-\frac{\pi r_c^2}{4r_c^{*2}}\right) = \exp\left[-\frac{\pi\gamma^2}{r_c^{*2}(KC_\infty - P_l)^2}\right] \tag{8}$$

This exponential relation bears a superficial resemblance to classical nucleation (see below), a result, however, which is due purely to the form of the Rayleigh distribution. Different distributions will result in different functionals. For example, we will also consider stretched-exponential or log-normal expressions of the form

$$f_q = \exp\left(-\frac{r_c^n}{\sigma r_c^{*n}}\right) \text{ or } f_q = \frac{1}{2}\operatorname{erfc}\left(\frac{\ln\frac{r_c}{r_c^*}}{\sqrt{2}\,\sigma}\right) \tag{9}$$

respectively, where n is a positive exponent and σ is a measure of the variance. The type of assumed distribution influences the results to be obtained, as will be demonstrated below. In comparing with the experimental results, we postulated a size distribution and then determined its parameters by fitting the experimental data.

As long as the level of supersaturation increases with time, the righthand side of Eq. 8 also increases, implying that additional sites become activated, and the nucleation fraction continuously rises. This is consistent with experimental evidence of sequential nucleation reported by Li and Yortsos (1995a), Hawes et al. (1997), Mackay et al. (1998), and Bora et al. (2000). After the supersaturation reaches a maximum (local or global), Eq. 8 predicts a decreasing f_q, which is unphysical. Therefore, in segments of decreasing supersaturation the nucleation fraction is assumed constant. When the supersaturation goes through a global maximum, it signals the end of the nucleation period, in which case the fraction of pores ultimately activated, f_{qf}, will be given by Eqs. 8 and 9 at the time of the maximum supersaturation.

The fraction f_{qf} can be directly related to the number of bubbles nucleated per unit pore volume, N_f, a quantity used in Firoozabadi and Kashchiev (1996) to quantify nucleation. Assuming $n_B = 1$, we have

$$N_f = \frac{f_{qf} N_T}{V_p} \tag{10}$$

where N_T is the total number of pores and V_p is the total pore volume. By noting that $V_p = N_T V_s$, where V_s is a typical volume of a pore (site), we can further write

$$N_f = \frac{f_{qf}}{V_s} \tag{11}$$

This allows us to relate the nucleation fraction to experimental values of N_f (see below). We note in advance that in typical experiments, f_{qf} is very small, of the order of 10^{-9}–10^{-6}.

A different approach is to use rate-dependent heterogeneous nucleation. Consider the nucleation-rate expression

$$\frac{dN_f}{dt} = K_{\text{het}} \exp\left[-\frac{16\pi\gamma^3 f}{3k_B T(KC_\infty - P_l)^2}\right] \tag{12}$$

where K_{het} is a heterogeneous rate constant, f is a dimensionless number expressing the wettability of the medium vis-a-vis nucleation (ranging between 1 and 0 for perfectly homogeneous and perfectly heterogeneous rate-dependent nucleation, respectively), and k_B is Boltzmann's constant. Both K_{het} and f can be determined from the matching of experimental data. Using the equivalent of Eq. 11, we can express Eq. 12 in terms of the nucleation fraction f_q

$$\frac{df_q}{dt} = \frac{K_{\text{het}} V_s}{n_B} \exp\left[-\frac{16\pi\gamma^3 f}{3k_B T(KC_\infty - P_l)^2}\right] \tag{13}$$

Compared to Eq. 8, Eq. 13 contains an explicit rate dependence, while the dependence on parameters, such as γ, is different from the previous model, as expected. Both these models will be considered below.

Through the nucleation process, nucleation centers are activated sequentially, giving rise to evolving gas clusters, which grow by mass transfer from the liquid to the gas. Sequential nucleation results in clusters of different ages (the time passed since a particular class of gas clusters has been nucleated/activated). Let $\omega(\tau)$ be the number density of clusters nucleated per total number of pores. Then, $\omega(\tau)d\tau$ is the number of new clusters per total number of pores that become activated in the time interval between τ and $\tau + d\tau$. Evidently

$$\omega(\tau)d\tau = n_B df_q \tag{14}$$

This relation will be used below to simplify the expressions for the gas-phase growth.

Gas-phase growth

During the growth of the gas phase, we can roughly distinguish two periods, one in which the growth is within single pores and another corresponding to gas clusters spanning several pores (Figures 2a and 2b, respectively). The first period extends throughout and following the nucleation stage, the second is the later stage of growth. In either, growth is driven by diffusive mass transfer of the dissolved gas. During the first period, mass transfer results mostly in the increase of the volume of the gas. During the second, it also leads to an increase in the gas pressure, in case the interface becomes pinned at pore throats (Figure 2) until the time when the smallest capillary threshold at the throats is overcome. Following this, the gas cluster volume expands accordingly. In general, different clusters compete for the available solute in the liquid, the relative mass-transfer rates depending on their geometry and relative position. These dynamics were analyzed in Li and Yortsos (1995a,b).

In the absence of competition between adjacent clusters, an isolated cluster j grows at a rate that is proportional to its effective radius, $R_j(t,\tau)$, and the driving force $C_\infty - C_i$, where C_∞ is the far-field concentration and C_i the equilibrium concentration at the gas–liquid interface. We will proceed, therefore, by assuming that the mass transfer is by quasi-steady-state diffusion and that the gas is ideal. Then we can write the following mass balance for a growing cluster

$$\left(\frac{M_w}{R_g T}\right)\frac{d}{dt}\left(P_l V_g\right) \approx 4\pi\lambda R_j\, \mathfrak{D}(C_\infty - C_i) \tag{15}$$

where M_w is the molecular weight of the gas, R_g the ideal gas constant, T the temperature, V_g the gas-cluster volume, and $\mathfrak{D}$ the diffusion coefficient. The mass-transfer term in Eq. 15 was obtained assuming quasi-steady-state diffusion to a spherical bubble. This is true even for ramified fractal clusters, as was verified by Satik and Yortsos (1996) for a percolation cluster. Dimensionless parameter λ is an $O(1)$ geometric constant to account for possible corrections to the mass-transfer model depending on the growth period (see below). In Eq. 15 we have neglected the capillary pressure, P_c, which in typical applications is small compared to the liquid pressure. From Henry's law, we also have

$$C_i = \frac{P_v}{K} = \frac{P_l + P_c}{K} \approx \frac{P_l}{K} \tag{16}$$

where the second equality is again an excellent approximation in the typical applications examined here.

The gas volume, V_g, takes a different expression in the two different periods. For growth within a single pore, $V_g \approx V_c(R_j/r_c^*)^3$, where V_c is a characteristic cavity volume (defined here as $4/3\pi r_c^{*3}$). For growth of a cluster spanning several pores, we have $V_g \approx A^* V_s(R_j/r_s^*)^{D_f}$, where V_s is the average site volume, r_s^* is a characteristic pore-body size, D_f is the mass fractal dimension, approximately equal to 2.5 for a 3-D cluster, and A^* is a dimensionless geometric prefactor. To capture both periods with the same equation, we write

$$\left(\frac{AV_c M_w}{R_g T}\right)\frac{d}{dt}\left[P_l\left(\frac{R_j}{r_c^*}\right)^{D_f}\right] = 4\pi\lambda R_j\, \mathfrak{D}(C_\infty - C_i) \tag{17}$$

with the understanding that D_f varies between 3 and 2.5, and A between 1 and $(A^* V_s/V_e)(r_c^*/r_s^*)^{D_f}$, during the nucleation period and growth periods, respectively.

The nucleation period and the early part of the growth period are adequately represented by Eq. 17. However, growth during the later stages of the second period, where gas clusters span several pores, cannot in reality be captured by Eq. 17. Competing clusters affect growth rates in a nontrivial manner. The latter would still be proportional to a mean driving force, $C_\infty - C_i$, where now C_∞ is the volume-averaged concentration in the liquid, and R_j stands for the average size of a cluster. However, the mass-transfer coefficient, λ, may be variable in time and space, while coalescence of clusters will also occur. Accounting for these complexities is a difficult problem, the solution of which requires a pore-network approach (Li and Yortsos, 1995a,b).

Under the preceding assumptions, the gas phase will be described as a collection of clusters of size $R(t,\tau)$, the dynamics of each of which is described by Eq. 17, with R_j replaced by R, namely,

$$\left(\frac{AV_c M_w}{R_g T}\right)\frac{\partial}{\partial t}\left[P_l\left(\frac{R}{r_c^*}\right)^{D_f}\right] = 4\pi\lambda R\, \mathfrak{D}(C_\infty - C_i) \tag{18}$$

subject to the initial condition $R(\tau,\tau) = r_c(\tau)$, where r_c satisfies Eq. 4. In the formulation of Firoozabadi and Kashchiev (1996), the equivalent of Eq. 18 was integrated under a number of simplifying assumptions to obtain an explicit dependence of R on time. Such an approximation is not used here.

Next, consider the mass balance for the solute in the liquid phase. We have

$$\frac{d}{dt}\left[V_p(1-S_g)C_\infty\right] = -4\pi\lambda\, \mathfrak{D}(C_\infty - C_i)N_T\int_0^t R(t,\tau)\,\omega(\tau)\ d\tau - C_\infty Q(t) \tag{19}$$

where the integration is over all existing clusters and $Q(t)$, the volumetric flow rate of the liquid out of the porous medium, is in general a function of time. Equivalently, we can rewrite Eq. 19 as

$$\frac{d}{dt}\left[V_p(1-S_g)C_\infty\right] = -4\pi\lambda\, \mathfrak{D}(C_\infty - C_i)N_T n_B\int_0^{f_q}\hat{R}(t,f)\ df - C_\infty Q(t) \tag{20}$$

where we introduced the notation $\hat{R}(t,f(\tau)) \equiv R(t,\tau)$ for the radius of a cluster at time t, nucleated when the nucleation fraction was $f(\tau)$. For the case of instantaneous nucleation, for example, as postulated in Firoozabadi and Kashchiev (1996), $\hat{R}(t,f_q) = R(t)\delta(f_q - f_{qf})$, where f_{qf} is the final nucleation fraction and δ is the Dirac delta function. Then, the preceding integral reduces to $R(t)f_{qf}$. However, f_{qf} is the very quantity we must determine, is not known *a priori*, and needs to be computed as part of the overall process, as discussed in detail below.

The volumetric flow rate $Q(t)/V_p$ is related to the pressure decline rate through the mass balance on the liquid, which reads

$$\frac{d}{dt}\left[\rho_l(1-S_g)\right] = -\rho_l\frac{Q(t)}{V_p} \tag{21}$$

Table 1. Characteristic Values of Various Parameters

Parameter	CPDR	CLWR
MW (g/mol)	18.6	16.0
D (cm^2/s)	2.40×10^{-5}	1.35×10^{-5}
γ (mN/m)	8.2	13.0
T (K)	314.6	314.6
P_b (MPa)	6.0	7.384
K (MPa·m^3/kg)	8.604×10^{-3}	1.537×10^{-1}
c (MPa^{-1})	1.45×10^{-3}	2.17×10^{-3}
r_s (cm)	9.0×10^{-4}	1.0×10^{-2}
r_c (cm)	8.0×10^{-6}	2.0×10^{-3}
A^*	1.	1.
n_B	1.	1.
λ	1.	1.
a (Pa/s)	26.82	—
Q (cm^3/s)	—	1.67×10^{-5}
V_p (cm^3)	—	132.24
Π_1	5.859×10^{-6}	—
Π_2	2.327×10^{6}	1.330×10^{3}
Π_3	8.700×10^{-3}	1.603×10^{-2}
Π_4	—	1.559×10^{-6}
Π_c	3.417×10^{-2}	1.760×10^{-4}

Note: CPDR: Constant pressure decline rate; CLWR: constant liquid withdrawal rate.

where ρ_l is the liquid density. For a slightly compressible liquid,

$$\rho_l = \rho_b \exp\left[c(P_l - P_b)\right] \tag{22}$$

where the liquid compressibility, c, takes values in the range $1.45\times10^{-4} - 1.45\times10^{-3}$ MPa^{-1}. Then

$$\frac{Q(t)}{V_p} = -(1-S_g)c\frac{dP_l}{dt} + \frac{dS_g}{dt} \tag{23}$$

Finally, the gas saturation is related to the radius of the growing clusters and the nucleation fraction through the relation

$$S_g = Av\int_0^t \left(\frac{R(t,\tau)}{r_c^*}\right)^{D_f} \omega(\tau)\ dt = Avn_B\int_0^{f_q}\left(\frac{\hat{R}(t,f_q)}{r_c^*}\right)^{D_f} df_q \tag{24}$$

where we introduced the volume ratio $v \equiv V_c/V_s$. This parameter can be calculated from the knowledge of the average cavity and pore sizes. Subject to the relevant initial conditions, the system of Eqs. 18, 20, 23, and 24 can be integrated. Integration proceeds until the time when the critical gas saturation (Eq. 1) is reached.

Dimensionless formulation and scaling

For the solution of the problem, we recast the equations in dimensionless form. Denote dimensionless quantities by subscript D and scale concentrations by $C_b = P_b/K$, pressure by P_b, where subscript b refers to the bubble point, and cluster size by r_c^*. The choice of the characteristic time depends on the process. We will take $t^* = P_b/a$, where a is the pressure decline rate, for the case of constant pressure decline rate and $t^* = V_p/Q$, for the case of liquid withdrawal at constant volumetric flow rate Q.

For the case of constant pressure decline rate, the dimensionless mass balances for the solute in the gas and liquid phase read

$$(1-t_D)\frac{\partial \hat{R}_D^{D_f}}{\partial t_D} = \frac{\Pi_2}{A\Pi_1}(C_{D\infty} - P_{Dl})\hat{R}_D + \hat{R}_D^{D_f} \tag{25}$$

and

$$(1-S_g)\frac{dC_{D\infty}}{dt_D} = -\frac{1}{\Pi_1}(C_{D\infty} - P_{Dl})\int_0^{f_q}\hat{R}_D(t_D,f_q)\,df_q - \Pi_3(1-S_g)C_{D\infty} \tag{26}$$

where we used the equilibrium relationship

$$C_{Di} = P_{Dl}(t_D) \tag{27}$$

and assumed that the process begins ($t_D = 0$) when the pressure is at the bubble point. In the preceding, we have defined three dimensionless groups,

$$\Pi_1 = \frac{V_p a}{4\pi\lambda\,\mathfrak{D}P_b N_T r_c^*} = \frac{V_s a}{4\pi\lambda\,\mathfrak{D}P_b n_B r_c^*}$$

$$\Pi_2 = \frac{R_g T}{v n_B M_w K},\ \text{and}\ \Pi_3 = cP_b \tag{28}$$

Parameter Π_1 expresses the ratio of the characteristic times for diffusion at the pore scale to that for the decline of pressure. Although a small number in typical applications (see Table 1), it plays a key role in determining the nucleation fraction and the critical gas saturation. Parameter Π_2 is the product of the geometric constant, vn_B, with a thermodynamic constant, expressing the ratio of the equilibrium concentrations in the liquid and the gas phases. These parameters are either known or can be estimated from comparison with experimental data.

For the case of constant liquid-withdrawal rate the analogous equations read

$$P_{Dl}(t_D)\frac{\partial \hat{R}_D^{D_f}}{\partial t_D} + \hat{R}_D^{D_f}\frac{dP_{Dl}}{dt_D} = \frac{\Pi_2}{A\Pi_4}(C_{D\infty} - P_{Dl})\hat{R}_D \tag{29}$$

and

$$(1-S_g)\frac{dC_{D\infty}}{dt_D} = -\frac{1}{\Pi_4}(C_{D\infty} - P_{Dl})\int_0^{f_q}\hat{R}_D(t,f_q)\ df_q - C_{D\infty} + C_{D\infty}\frac{dS_g}{dt_D} \tag{30}$$

where

$$\Pi_4 = \frac{Q}{4\pi\lambda\, \mathfrak{D} N_T n_B r_c^*} = \frac{V_s Q}{4\pi\lambda\, \mathfrak{D} V_p n_B r_c^*} \tag{31}$$

Here, parameter Π_4 expresses the ratio of the characteristic time for diffusion to that for the emptying of the pore volume. Typically, this is also a small number (Table 1). As will be shown below, Π_4/Π_3 plays a role equivalent to Π_1.

Finally, in both cases, we have the following relations: the liquid mass balance becomes

$$\frac{dP_{Dl}}{dt_D} = \frac{1}{\Pi_3(1-S_g)}\left(\frac{dS_g}{dt_D} - 1\right) \tag{32}$$

The gas saturation is

$$S_g = A\upsilon n_B \int_0^{f_q} \hat{R}(t_D, f_q)^{D_f}\ df_q \tag{33}$$

The cavity size that becomes activated at a given time is

$$r_{Dq} = \frac{\Pi_c}{C_{D\infty}(t_D) - P_{Dl}(t_D)} \tag{34}$$

where we introduced the dimensionless cavity capillary pressure threshold, $\Pi_c = (2\gamma \cos\theta)/(r_c^* P_b)$. The latter is an important parameter in the overall dynamics. In terms of the supersaturation

$$s \equiv C_{D\infty}(t_D) - P_{Dl}(t_D) \tag{35}$$

or, more conveniently, in terms of the rescaled supersaturation

$$s_D \equiv \frac{s}{\Pi_c} \tag{36}$$

Equation 34 can be further expressed as $r_{Dq} = s_D^{-1}$. The nucleation fraction is then given by the various expressions

$$f_q = \exp\left(-\frac{\pi}{4s_D^2}\right),\ f_q = \exp\left(-\frac{1}{\sigma s_D^n}\right),\ f_q = \frac{1}{2}\operatorname{erfc}\left(-\frac{\ln s_D}{\sqrt{2}\,\sigma}\right) \tag{37}$$

depending on the size distribution used, or by

$$\frac{df_q}{dt_D} = h_1 \exp\left(-\frac{h_2}{s^2}\right) \tag{38}$$

in the rate-dependent nucleation case. In the latter we introduced the dimensionless parameters

$$h_1 = \frac{K_{\text{het}} t^* V_s}{n_B} \text{ and } h_2 = \frac{16\pi\gamma^3 f}{3P_o^2 k_B T} \tag{39}$$

Parameter h_1 is inversely proportional to Π_1 or Π_4. If this dependence is extracted, then Eq. 39 reads as

$$h_1 = \frac{\zeta}{\Pi_1} \text{ or } h_1 = \frac{\zeta}{\Pi_4},\text{ where } \zeta \equiv \frac{K_{\text{het}} V_s^2}{4\pi\lambda\, \mathfrak{D} n_B^2 r_c^*} \tag{40}$$

The initial conditions for the simulations were $C_{D\infty} = 1$, $P_{Dl} = 1$, and $R_D(\tau,\tau) = s_D^{-1}(\tau)$.

The preceding system contains one key parameter, Π_1 or Π_4, describing the effect of the rate of increase of the supersaturation. Because it is small, a further rescaling of the nucleation fraction and the cluster size is necessary. After some analysis, it is not difficult to show that for the cavity nucleation model, the following scaling is valid (for example, for the constant pressure decline rate), $f_q \sim \Pi_1^{D_f/(D_f-1)}$ and $f_q R^{D_f} \sim O(1)$ (where, given that the nucleation fraction varies only during the first period, $D_f = 3$). This scaling contains the main effect of the pressure decline rate on the nucleation fraction. Thus, we can define a rescaled nucleation fraction

$$\phi_q = f_q \Pi_1^{-3/2} \text{ or } \phi_q = f_q\left(\frac{\Pi_4}{\Pi_3}\right)^{-3/2} \tag{41}$$

and rescaled cluster sizes

$$\rho_D = \Pi_1^{1/2}\hat{R}_D \text{ or } \rho_D = \left(\frac{\Pi_4}{\Pi_3}\right)^{1/2}\hat{R}_D \tag{42}$$

in the two different cases. In the new notation, the governing equations become as follows:

For the case of constant rate of pressure decline

$$(1-t_D)\frac{\partial \rho_D^{D_f}}{\partial t_D} = \frac{\Pi_2}{A}s\rho_D + \rho_D^{D_f} \tag{43}$$

and

$$(1-S_g)\frac{ds}{dt_D} = -s\int_0^{\phi_q}\rho_D(t_D,\phi_q)\ d\phi_q - (s+1-t_D)\left[\Pi_3(1-S_g)\right] + 1 - S_g \tag{44}$$

while for the constant liquid withdrawal rate,

$$\Pi_3 P_{Dl}(t_D)\frac{\partial \rho_D^{D_f}}{\partial t_D} + \Pi_3\,\rho_D^{D_f}\frac{dP_{Dl}}{dt_D} = \frac{\Pi_2}{A}s\rho_D \tag{45}$$

and

$$\Pi_3(1-S_g)\frac{ds}{dt_D} = -s\int_0^{\phi_q}\rho_D(t_D,\phi_q)\ d\phi_q + \left(\frac{dS_g}{dt_D} - 1\right)\left[\Pi_3(P_{Dl}+s) - 1\right] \tag{46}$$

The last two equations are also accompanied by Eq. 32. The gas saturation expression for either case becomes

$$S_g = Avn_B \int_0^{\phi_q} \rho\left(t_D, \phi_q\right)^{D_f} \, d\phi_q \tag{47}$$

For the case of rate-dependent nucleation, the rescaled nucleation fraction reads as

$$\frac{d\phi_q}{dt_D} = h_1^* \exp\left(-\frac{h_2}{s^2}\right) \tag{48}$$

where $h_1^* = h_1 \Pi_1^{-3/2}$ or $h_1^* = h_1(\Pi_4/\Pi_3)^{-3/2}$ in the respective cases. The solution of the system of the rescaled equations will be sought numerically in the following sections.

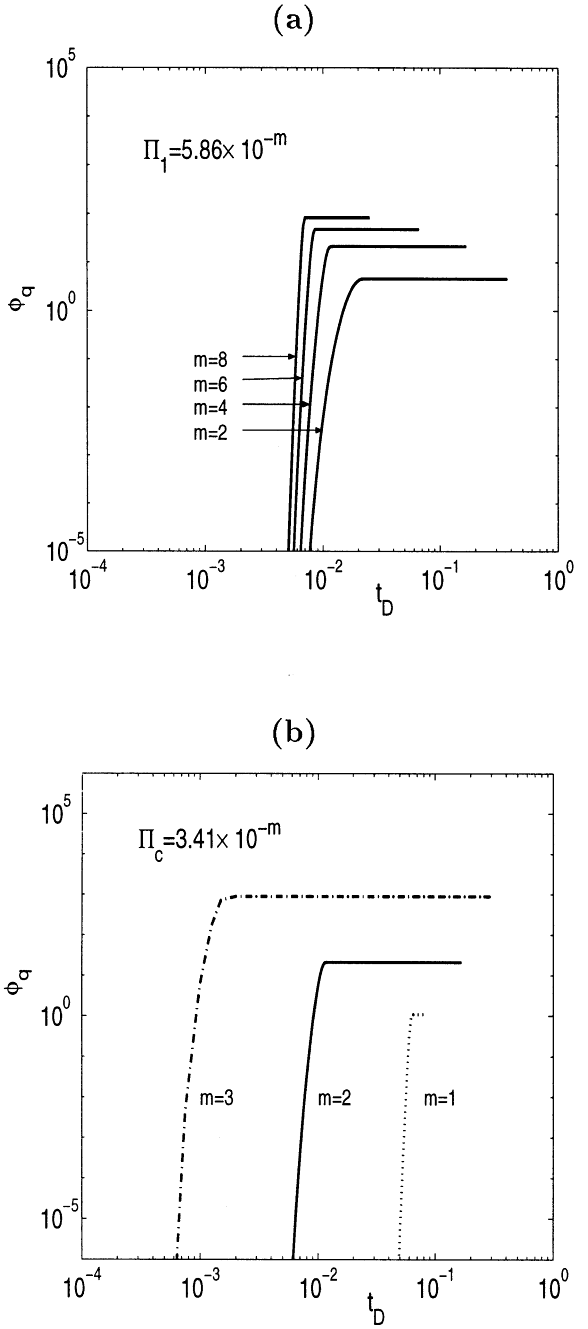

Figure 4. Variation of the rescaled nucleation fraction, ϕ_q, as a function of the dimensionless time, t_D.

(a) Effect of $\Pi_1 = 5.86 \times 10^{-m}$, for $\Pi_c = 3.41 \times 10^{-2}$, $\Pi_2 = 2.33 \times 10^6$, and $\Pi_3 = 8.7 \times 10^{-3}$. (b) Effect of $\Pi_c = 0.34 \times 10^{-m}$, for $\Pi_1 = 5.86 \times 10^{-4}$ and $\Pi_3 = 8.7 \times 10^{-3}$.

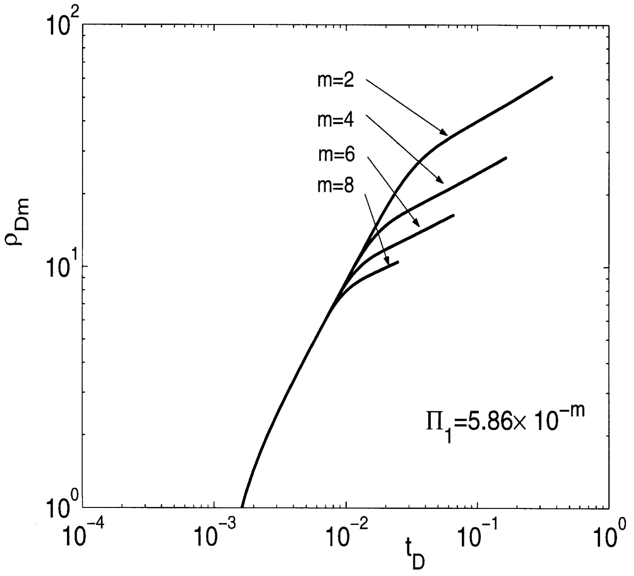

Figure 5. Variation of the mean rescaled dimensionless radius, ρ_{Dm}, as a function of the dimensionless time, t_D.

Effect of $\Pi_1 = 5.86 \times 10^{-m}$, for $\Pi_c = 3.41 \times 10^{-2}$, $\Pi_2 = 2.33 \times 10^6$, and $\Pi_3 = 8.7 \times 10^{-3}$.

Numerical Results

The system of differential equations was solved numerically using a fourth-order Runge–Kutta method (Press et al., 1994). A typical calculation requires the time to be marched forward. A difficulty is that the total number of classes of gas clusters is not known *a priori*, but it is an outcome of the computation during the nucleation process. In theory, this number is infinite, and the problem becomes one of solving an infinite system of differential equations. In practice, the number of equations is constrained by the size of the time step. At each time step we examine whether nucleation of a new class of gas clusters is possible, namely whether the supersaturation is increasing. If so, a new class of gas clusters is added. Then, the simultaneous growth of all different classes of clusters is computed. When the supersaturation reaches a maximum, further nucleation stops. Computations during the nucleation process were also facilitated with an asymptotic analysis, to be described in more detail later.

Constant pressure decline rate

In the typical case, parameters that can vary over a significant range are Π_1 and Π_c (and possibly Π_2). An additional variable is the type of the cavity-size distribution used in the calculation of the nucleation fraction. The sensitivity of these parameters are examined in the simulations.

The effect of Π_1 and Π_c on the rescaled nucleation fraction, ϕ_q, the mean rescaled radius, $\rho_{D,m}$, the rescaled supersaturation, s_D, and the gas saturation, S_g, is shown in Figures 4–7. In these calculations, we used a Rayleigh cavity-size distribution, Π_2 and Π_3 were kept constant to the values 2.33×10^6 and 8.7×10^{-3}, respectively, while Π_1 varied over several orders of magnitude (from 10^{-8} to 10^{-2}).

The variation of ϕ_q as a function of the dimensionless time, t_D, and of the parameters Π_1 and Π_c is shown in Figure 4. It is found that ϕ_q increases very rapidly in a small time interval, and then stabilizes to a final value at the conclusion of nucleation. Such behavior is characteristic of nucleation processes, and has features similar to those reported by El Yousfi et al. (1991, 1997). It is demonstrated here for the first time for the case of nucleation from preexisting, trapped gas. The rapid variation of ϕ_q is approximately a stretched exponential of the form

$$\phi_q \sim \exp\left(-\frac{\pi\Pi_c^2}{4t_D^2}\right), \quad \phi_q \sim \exp\left(-\frac{\Pi_c^n}{\sigma t_D^n}\right), \quad \phi_q \sim \operatorname{erfc}\left(\frac{\ln\dfrac{\Pi_c}{\sigma t_D}}{\sqrt{2}\,\sigma}\right) \tag{49}$$

for the different cases, as during the early nucleation period we have $s \sim t_D$ (see below). Equation 49 suggests that, for example, for the Rayleigh distribution case, a plot of $-\ln\phi_q$ vs. t_D^{-2} is linear with slope $\pi\Pi_c^2/4$. Because of the resulting very sharp rise, this process can be interpreted as instantaneous nucleation (IN). However, proceeding with such an assumption does not allow for the computation of the final nucleation values. Instead, we must consider the details of the approach to the final values using the progressive nucleation model, used here. Figure 4a shows that for constant Π_c, the effect of Π_1 on the rescaled nucleation fraction is not very significant at small Π_1, but that it becomes stronger (roughly

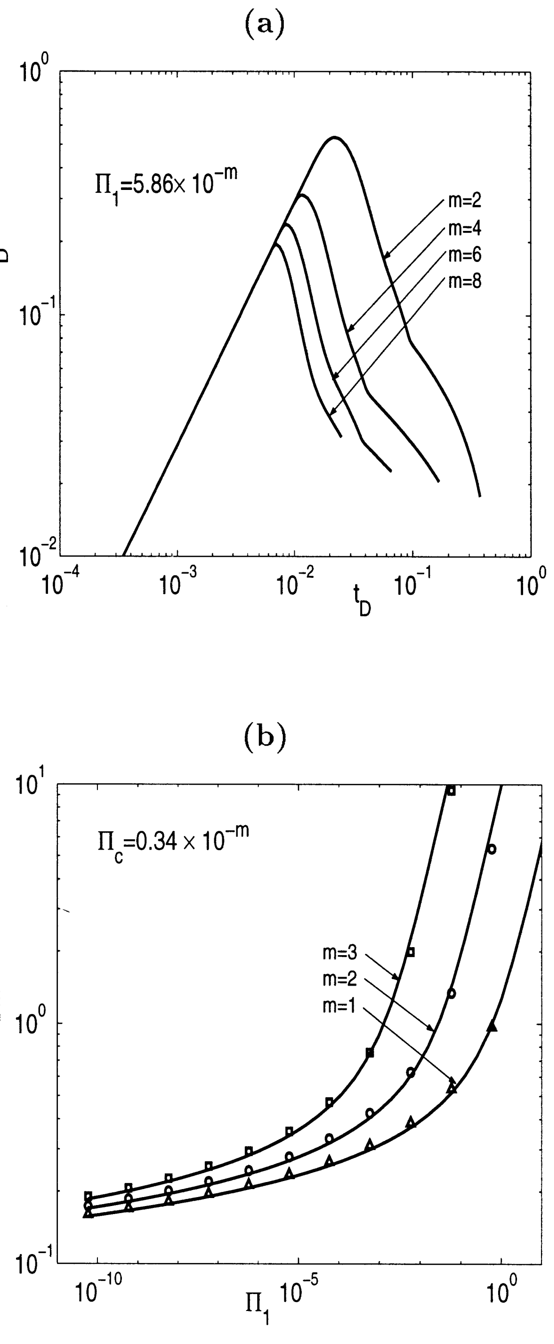

Figure 6. Numerical results for the supersaturation.

(a) Variation of the rescaled supersaturation, s_D, as a function of the dimensionless time, t_D; effect of $\Pi_1 = 5.86\times 10^{-m}$, for $\Pi_c = 3.41\times 10^{-2}$, $\Pi_2 = 2.33\times 10^6$, and $\Pi_3 = 8.7\times 10^{-3}$: (b) the effect of the dimensionless parameter Π_1 on the maximum rescaled supersaturation, s_{Dm}, for $\Pi_c = 0.34\times 10^{-m}$; points correspond to the full numerical solution, solid lines correspond to the simpler model.

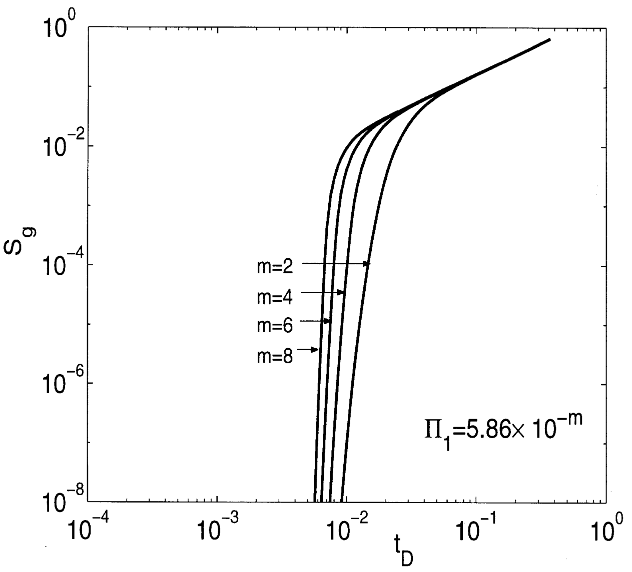

Figure 7. Variation of the gas saturation, S_g, as a function of the dimensionless time, t_D.

Effect of $\Pi_1 = 5.86\times 10^{-m}$, for $\Pi_c = 3.41\times 10^{-2}$, $\Pi_2 = 2.33\times 10^6$, and $\Pi_3 = 8.7\times 10^{-3}$.

a power law) as Π_1 takes larger values. The relatively weak dependence on Π_1 verifies the correctness of the scaling (Eq. 41). At the same time, the stronger dependence at larger Π_1 is significant, and as shown below, is needed in order to explain experimental data. In terms of the actual nucleation fraction, these findings imply that an increase in Π_1 leads to an increase in the final nucleation fraction, f_{qf}, according to a power-law scaling, namely $f_{qf} \sim \Pi_1^{3/2}$ at very small Π_1, and $f_{qf} \sim \Pi_1$ at larger Π_1. The effect of Π_c is also significant. As Π_c increases, the final rescaled nucleation fraction ϕ_{qf} (hence, f_{qf}) decreases (Figure 4b). The increase of f_{qf} with an increase in Π_1 and a decrease in Π_c is expected. Larger values of Π_1 result from a faster decline rate, a greater departure from equilibrium, the establishment of a greater supersaturation, and, hence, the activation of more nucleation sites. Likewise, smaller Π_c imply that nucleation is facilitated at increasingly smaller supersaturations, as larger size cavities can be activated. The approximate analysis shown below will provide an explanation of the behavior observed.

Figure 5 shows the corresponding effects on the mean rescaled size ρ_{Dm}. There are two regions, one corresponding to the nucleation period, and another to growth after nucleation. The two periods can be roughly approximated as power-law regimes (as a function of time) with slopes approximately equal to 1 and 0.63, respectively. The effect of Π_1 is relatively insignificant at small Π_1, confirming the validity of the scaling (Eq. 41). The effect of Π_c is more significant. Smaller values of Π_c lead to an increase in the nucleation fraction, and a corresponding decrease in the size of the gas clusters at the conclusion of nucleation.

Figure 6a shows plots of the rescaled supersaturation s_D as a function of time for different Π_1 and Π_c. At the beginning of the process and during nucleation, the supersaturation increases with time almost linearly, suggesting that $C_{D\infty}$ does not vary significantly in that period. As nucleation and growth take place, the rate of supersaturation increase slows down and at some point, s_D reaches a maximum value, s_{Dm}. It is at that point where nucleation terminates. Following this point, the supersaturation decreases monotonically. The value s_{Dm} is plotted in Figure 6b as a function of Π_1 and Π_c. Note that s_{Dm} is in general of the order of 10^{-1}. The dependence on the parameters is weak at small Π_1 and large Π_c, but becomes stronger at larger Π_1 and smaller Π_c. This behavior is consistent with that of the nucleation fraction discussed earlier. From a compilation of experimental results Scherpenisse et al. (1994) suggested that s_{Dm} behaves roughly as a power law of the pressure decline rate with exponent 1/4. Our analysis indicates that such a power law is not universally valid, although it may apply in a certain range of Π_1. It is interesting that the sensitivity of s_{Dm} to Π_c and Π_1 (and in particular to the latter) is not as large as one might have intuitively anticipated. Nonetheless, its effect on the nucleation fraction can be significant, due to the exponential dependence, as can be seen, for example, in the following expression (for a Rayleigh distribution)

$$\phi_q = \exp\left[-\frac{\pi}{4s_D^2} - \frac{D_f}{(D_f-1)}\ln \Pi_1\right] \tag{50}$$

Because of the exponential dependence on s_D^{-2} and because s_{Dm} is of the order of 10^{-1}, even small changes in s_D have a very large effect on the nucleation fraction. This large sensitivity counterbalance the weak sensitivity of s_{Dm} on Π_1 and β and leads overall to a nontrivial effect.

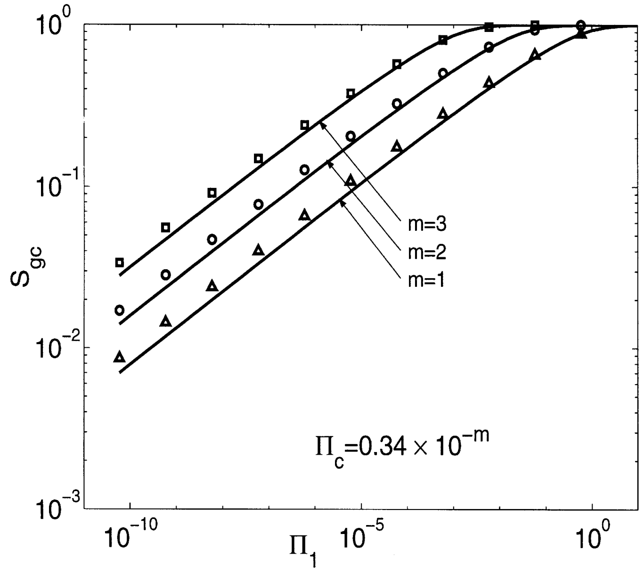

Figure 8. The effect of the dimensionless parameter Π_1 on the critical gas saturation, S_{gc}, for $\Pi_c = 0.34 \times 10^{-m}$.

Points denote the full numerical solution; solid lines correspond to the simpler model.

The evolution of the gas saturation is shown in Figure 7. It follows that of f_q, during the nucleation period, and that of ρ_{Dm}, during the period of growth. The latter gives a power-law segment of slope 0.63. The effect of Π_c is indirect, in that smaller values of Π_c promote larger values of S_g due to an increase in both f_{qf} and ρ_D. The difference between equilibrium and actual curves depends on the value of Π_1, increasing as the latter increases, but remaining constant following the end of nucleation. Figure 8 shows the effects of Π_1, and Π_c on the critical gas saturation S_{gc}. In our work, the latter pertains to the formation of a sample-spanning cluster, in the absence of viscous or gravity effects. Thus, Figure 8 actually reflects the variation of f_{qf}. Figure 8 shows that S_{gc} can be considered a power-law both of Π_1 and of Π_c with exponents that vary between 0.16 and 0.25 with respect to Π_1 and between -0.33 and -0.22, with respect to Π_c, respectively. The trends are consistent with the experimental evidence (Scherpenisse et al., 1994; Bora et al., 2000). In Figure 8 we allowed S_{gc} to take values that, in the case of high depletion rates, may be larger than what is required for the validity of our model. This was done only for the sake of parametric sensitivity.

Constant rate of liquid withdrawal

Except for the evolution of pressure with time, similar results are obtained for the case of constant rate of liquid withdrawal. The effect of the parameters is also very similar to the constant pressure decline rate, subject to the change $\Pi_1 \rightarrow \Pi_4/\Pi_3$ and to the rescaling of time by Π_3. Thus, we anticipate a scaling of the form: $f_{qf} \sim \Pi_4^{3/2}$ at small Π_4, and $f_{qf} \sim$

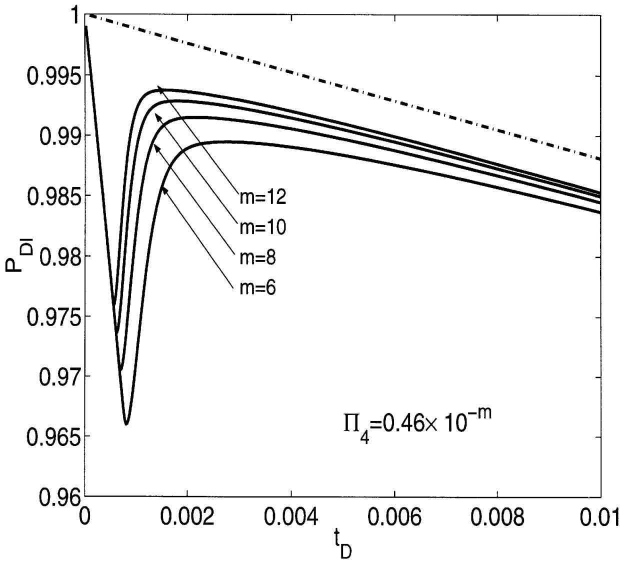

Figure 9. Variation of the dimensionless pressure, P_{Dl}, as a function of the dimensionless time, t_D, for the case of constant liquid withdrawal rate.

Effect of $\Pi_4 = 0.4631\times10^{-m}$, for $\Pi_c = 1.67\times10^{-1}$, $\Pi_2 = 6.84\times10^5$, and $\Pi_3 = 1.52\times10^{-2}$. Shown in dashed-dotted line is the thermodynamic equilibrium curve.

Π_4 at larger Π_4; and of the form: $f_{qf} \sim \Pi_c^{-2}$ at large Π_c, and $f_{qf} \sim \Pi_c^{-1.3}$ at smaller Π_4. The critical gas saturation has the analogous scaling: $S_{gc} \sim \Pi_4^{0.25}$ at small Π_4, and $S_{gc} \sim \Pi_4^{0.16}$ at larger Π_4; and $S_{gc} \sim \Pi_c^{-0.22}$ at larger Π_c, and $S_{gc} \sim \Pi_c^{-0.33}$ at smaller Π_4. The discussion and interpretation of the findings is similar to the case of constant pressure decline rate and will not be elaborated further. Additional figures and discussion are presented in Tsimpanogiannis (2002).

What is different in the case of constant rate of liquid withdrawal, is the evolution of pressure with time (Figure 9). In the calculations shown in Figure 9 we used a Rayleigh cavity-size distribution, Π_2 and Π_3 were kept constant to the values 6.84×10^5 and 1.5×10^{-2}, respectively, while Π_4 varied over several orders of magnitude (from 10^{-12} to 10^{-6}). During the nucleation period, the pressure declines almost linearly with time, $P_{Dl} \approx 1 - t_D/\Pi_3$, following Eq. 32. This decrease slows down as nucleation sets in, and when the maximum supersaturation is approached, the pressure reaches a local minimum. Following this minimum, the pressure increases, reaches a maximum, and subsequently decreases, roughly paralleling the equilibrium curve. The pressure minimum decreases as Π_4 increases (Figure 9), the dependence being roughly the same as that of s_{Dm}, namely weak at small Π_4 and stronger at larger Π_4 (where the 1/4 power law may be applicable).

The nonequilibrium behavior reflects the competition between mass transfer and solute availability and can be explained as follows. The ideal gas law requires $P_gV_g = nR_gT$. The rate of change, dn/dt, of the moles in the gas phase is dictated by the mass-transfer rate. At the end of the nucleation period, near s_{Dm}, this rate is the highest. Now, if the rate by which the gas volume expands, dV_g/dt (which is almost equal to Q), is not sufficiently large, the increase in volume due to mass transfer cannot be compensated, thus, the pressure, P_g, must increase. An increasing pressure leads to a successively decreasing supersaturation (since C_i increases), thus, to a continuous decrease of the mass-transfer rate. Eventually, this decrease becomes sufficiently large for the volume expansion rate to balance mass transfer. Then, the pressure goes through a maximum, following which it begins to decline.

In the preceding, we used the cavity-based nucleation model. We must stress that qualitatively similar results were obtained for the model based on rate-dependent nucleation. These will not be shown. In a later section, the numerical solutions obtained will be compared against available experimental results. However, before doing so it is beneficial to provide an interpretation of the main findings, using a simpler model.

Interpretation Using a Simpler Model

To interpret the results obtained we consider a simpler model that captures the essential features of the problem. Consider, first, the nucleation period.

Nucleation

Constant Pressure Decline Rate. To approximately describe the nucleation period, we simplify as follows the equations for the gas-phase growth and the supersaturation

$$\frac{\partial \rho_D^3}{\partial t_D} \approx \Pi_2 s \rho_D \qquad (51)$$

and

$$\frac{ds}{dt_D} \approx 1 - s\int_0^{\phi_q(s)} \rho_D \, d\phi_q \qquad (52)$$

respectively. These are subject to the initial conditions

$$s(0) = 0 \text{ and } \rho_D(\tau,\tau) = \frac{\Pi_1^{1/2}}{s_D(\tau)} \qquad (53)$$

At early times and for small Π_1, the approximate solution of Eqs. 51–53 is

$$s \approx t_D \text{ and } \rho_D \approx \left[\frac{\Pi_1\Pi_c^2}{s^2(\tau)} + \frac{\Pi_2\left[s^2 - s(\tau)^2\right]}{3}\right]^{1/2} \qquad (54)$$

The dimensionless supersaturation is equal to the dimensionless time and the mean cluster size becomes eventually a power law of time with exponent 1. These results are consistent with the numerical results during the nucleation period (Figures 5 and 6).

We will use Eq. 52 to approximate the approach to the maximum supersaturation. The latter is reached when ds/dt_D

= 0, namely, when

$$s\int_0^{\phi_q}\rho_D \, d\phi_q \approx 1 \tag{55}$$

From Eq. 54 we approximately read $\rho_D \approx (\Pi_2/3)^{1/2} s(t_D)$. Then, using the definition of ϕ_q leads to an algebraic equation for the rescaled maximum supersaturation, s_{Dm}. For example, for the case of Rayleigh distribution, we have the equation

$$\frac{\pi}{4s_{Dm}^2} - 2\ \ln\ s_{Dm} \approx \ln\ \Lambda - \frac{1}{2}\ln 3 - \frac{3}{2}\ln\ \Delta \tag{56}$$

where we introduced the combination of variables

$$\Delta \equiv \Pi_1 \Pi_c^{-4/3} \Pi_2^{-1/3} \tag{57}$$

and for the case of constant pressure decline rate, $\Lambda \equiv 1$. Likewise, for the case of a stretched exponential, and of a log-normal distribution, we have

$$\sigma^{-1} s_{Dm}^{-n} - 2\ \ln\ s_{Dm} \approx \ln\ \Lambda - \frac{1}{2}\ \ln\ 3 - \frac{3}{2}\ \ln\ \Delta \tag{58}$$

$$s_{Dm}^2 \operatorname{erfc}\left(\frac{\ln \dfrac{1}{s_{Dm}}}{\sqrt{2}\,\sigma}\right) \approx 2\sqrt{3}\,\Delta^{3/2}\Lambda^{-1} \tag{59}$$

where, again, for the constant pressure decline rate, $\Lambda = 1$. Equations 56–59 represent key findings of this article. First, they suggest that the dependence of the maximum supersaturation on the various parameters, other than the thermodynamic ones, enters only through Δ. The solution of Eq. 56 for the Rayleigh distribution is plotted in Figure 10, as a function of Δ. We see that s_{Dm} varies weakly, in the range 0.1–1, as Δ varies over several orders of magnitude (between 10^{-10} and 10^3). For small Δ, the maximum supersaturation is practically constant. As Δ takes larger values, s_{Dm} increases weakly and eventually more strongly, as Δ approaches the order of one (compare also with Figure 6). Also shown in the logarithmic coordinates of Figure 10 is a line with slope 1/4, corresponding to the 1/4 power law postulated by Scherpenisse et al. (1994) to describe several experimental data. Although the power law does not capture the overall behavior, it can approximate the results in a certain window of Δ. Also plotted in the same figure are the results of the numerical solution of the full problem for a number of different parameter values. The agreement between the numerical results and the simple analytical model is remarkable and demonstrates the validity of the simple Eq. 56. For the stretched exponential nucleation model, the variation is much stronger in the logarithmic plot. The solution of Eqs. 56, 58, and 59 corresponding to different distributions was investigated in detail in Tsimpanogiannis (2002). As the tail of the cavity-size distribution becomes longer (which occurs for smaller values of $n > 0$ and/or for larger σ) the dependence of s_{Dm} on Δ becomes stronger. In addition, the region where a power-law scaling with exponent $\approx 1/4$ tentatively fits the results, increases, and also corresponds to a range with smaller values of Δ.

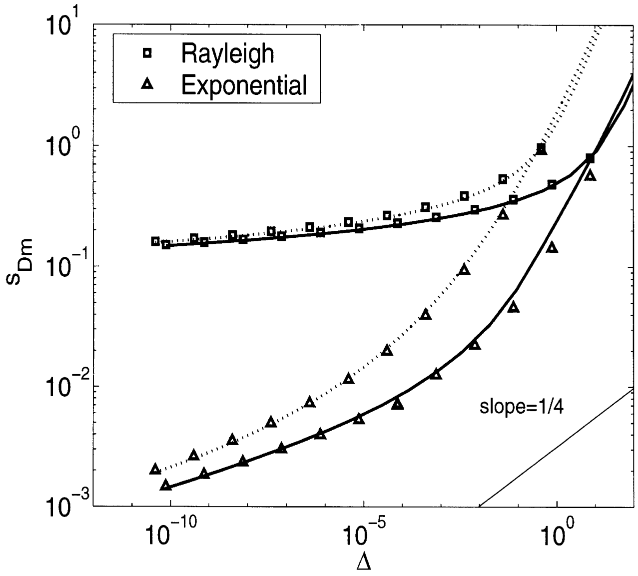

Figure 10. Maximum rescaled supersaturation, s_{Dm}, as a function of Δ for the cases of constant pressure decline rate (dotted lines) and constant liquid withdrawal rate (solid lines).

Comparison between the simpler model (dotted or solid lines) and the full numerical solution (denoted by triangles for the stretched exponential cavity-size distribution with $n = 0.5$ and $\sigma = 1.0$, and by squares for the Rayleigh cavity-size distribution).

Equations 56–59 can be used to approximate the final nucleation fraction, ϕ_{qf}, and the time (or pressure) at the end of nucleation. For all cases we have

$$\phi_{qf} \approx s_{Dm}^{-2} \Pi_c^{-2} \left(\frac{\Pi_2}{3}\right)^{-1/2} \Lambda^{-1} \tag{60}$$

thus, the final nucleation fraction reads

$$f_{qf} \approx s_{Dm}^{-2} \Pi_1^{3/2} \Pi_c^{-2} \left(\frac{\Pi_2}{3}\right)^{-1/2} \Lambda^{-1} \tag{61}$$

This equation represents another important result of this article and leads to the following conclusions:

1. In the region where s_{Dm} varies weakly with Δ (at small Δ) the final nucleation fraction varies as a power law of Π_1, with slope equal to 3/2. This is consistent with the anticipated increase in the nucleation fraction as the rate of pressure decline increases. The equation suggests a power-law dependence on the capillary properties of the cavity. One should interpret this carefully, however, since information on the cavity properties is included in all three parameters Π_1, Π_2, and Π_c (through r_c^* and υ). For example, if we were to consider only the dependence on r_c^*, we would find the power-law scaling $f_{qf} \sim r_c^{*2}$, indicating a smaller nucleation fraction as the cavity size decreases. This is as expected.

2. In the region where s_{Dm} can be approximated by a power-law dependence on Δ, for example, as $s_{Dm} \sim \Delta^m$, we have the scaling

$$f_{qf} \sim \Delta^{(3/2)-2m} \tag{62}$$

Such a dependence on Δ leads to a decrease in the exponent in the power-law scaling of f_{qf} on Π_1. For example, if we take $m \approx 1/4$ (as suggested by Scherpenisse et al., 1994), we read

$$f_{qf} \sim \Pi_1 \text{ and } f_{qf} \sim r_c^{*\,4/3} \tag{63}$$

A linear dependence of the rate of Π_1 was postulated in Scherpenisse et al. (1994) and McDougall and Sorbie (1999), to fit available experimental data.

3. The time, hence, the pressure, P_m, when nucleation ends can be approximated by using Eq. 54. We find

$$\frac{P_b - P_m}{P_b} \approx \Pi_c s_{Dm} \tag{64}$$

thus, the supersaturation at the end of nucleation is directly related to s_{Dm}. It follows that in the region where s_{Dm} is insensitive to Δ, the pressure supersaturation varies only linearly with Π_c. A rate dependence, observed experimentally in some cases, enters only insofar as s_{Dm} varies with Δ. Assuming again a power-law variation with $m \approx 1/4$, the maximum pressure supersaturation varies as follows

$$\frac{P_b - P_m}{P_b} \sim \Pi_1^{1/4} \text{ and } \frac{P_b - P_m}{P_b} \sim r_e^{-\,2/3} \tag{65}$$

The 1/4 power-law dependence was found to fit experimental data well (see below). It is interesting that the maximum supersaturation relative to the bulk bubble point is only weakly dependent on the rate of pressure decline, for example, varying by only a factor of 2 when the pressure decline rate varies by two orders of magnitude, in the range considered.

Constant Rate of Liquid Withdrawal. A similar analysis applies for the case of constant liquid withdrawal. After various simplifications, the equations for the gas phase growth and the supersaturation read

$$\Pi_3 \frac{d\rho_D^3}{dt_D} \approx \Pi_2 s \rho_D \tag{66}$$

and

$$\Pi_3 \frac{ds}{dt_D} \approx 1 - \left(1 + \frac{\kappa}{\Pi_3} - \kappa\right) s \int_0^{\phi_q} \rho_D \; d\phi_q \tag{67}$$

respectively, where we have introduced the thermodynamic parameter $\kappa \equiv (R_g T)/(M_w K)$. These are subject to the initial conditions

$$s(0) = 0 \text{ and } \rho_D(\tau,\tau) = \frac{\left(\dfrac{\Pi_4}{\Pi_3}\right)^{1/2}}{s_D(\tau)} \tag{68}$$

At early times and for small Π_4/Π_3, the solution is

$$s \approx \frac{t_D}{\Pi_3} \text{ and } \rho_D \approx \left[\frac{\Pi_4}{\Pi_3}\frac{\Pi_c^3}{s^2(\tau)} + \frac{\Pi_2\left[s^2 - s(\tau)^2\right]}{3}\right]^{1/2} \tag{69}$$

The early-time behavior is identical to the constant pressure decline rate, if t_D is replaced by t_D/Π_3 and Π_1 with Π_4/Π_3. We note again that the linear scaling of the cluster size with time is consistent with the full numerical solution.

Proceeding as previously, we find that the maximum rescaled supersaturation, s_{Dm}, is now given by

$$s \rho_D \phi_q \approx \frac{\Pi_3}{\kappa} \tag{70}$$

where ρ_D satisfies Eq. 69. Thus, the solution of Eq. 70 is the same as that obtained for the constant pressure decline rate problem, except that one must replace Π_1 with Π_4/Π_3, and take $\Lambda \equiv \kappa/\Pi_3$. For exactly the same reasons, the final nucleation fraction can be directly obtained from Eq. 61. The previous analysis for the constant pressure decline rate applies directly to the constant rate of liquid withdrawal, subject to the aforementioned substitution.

A comparison between the solution of the full problem (for the cases of the Rayleigh distribution and a stretched exponential with $n = 0.5$ and $\sigma = 1.0$) and of the approximate equation (Eq. 70) is also shown in Figure 10. We note an excellent agreement. The scalings obtained are also consistent with the solution of the full equations. Additional comparisons with stretched exponential cavity size distribution, which have lower values of n and σ, will be presented below.

As noted earlier, a difference for the problem involving a constant rate of liquid withdrawal is that the pressure reaches a local minimum. To identify it, we proceed as follows. Integrating Eq. 32, we obtain

$$\Pi_3 P_{Dl} \approx Av \phi_q \rho_D^3 - t_D + \Pi_3 \tag{71}$$

where we made the same approximation for the integral as in Eq. 67. Finding the minimum in pressure requires equating the derivative of Eq. 71 to zero. Using Eq. 69 for ρ_D, it is not difficult to show that the following equation is satisfied by the supersaturation s_{Dn} at that point

$$\phi_q\left(3s_{Dn}^2 + \frac{\pi}{2}\right) \approx \frac{\Pi_3}{Av}\left(\frac{3}{\Pi_2}\right)^{3/2}\left(\frac{1}{\Pi_c}\right)^2 \tag{72}$$

where we used a Rayleigh distribution. For the stretched exponential case we have

$$\phi_q\left(3s_{Dn}^2+\frac{ns_{Dn}^{2-n}}{\sigma}\right)\approx\frac{\Pi_3}{Av}\left(\frac{3}{\Pi_2}\right)^{3/2}\left(\frac{1}{\Pi_c}\right)^2 \tag{73}$$

Based on these equations, one can show that the pressure reaches its local minimum before the supersaturation reaches its maximum, suggesting that nucleation continues slightly after the minimum in pressure, albeit for a very brief period of time. We can solve the preceding to determine the pressure minimum. For the Rayleigh distribution, we approximately find

$$\frac{P_b-P_n}{P_b}\approx\Pi_c s_{Dn}\left(\frac{2s_{Dn}^2+\frac{\pi}{2}}{3s_{Dn}^2+\frac{\pi}{2}}\right) \tag{74}$$

and for the stretched exponential

$$\frac{P_b-P_n}{P_b}\approx\Pi_c s_{Dn}\left(\frac{2\sigma s_{Dn}^n+n}{3\sigma s_{Dn}^n+n}\right) \tag{75}$$

Given that s_{Dn} is generally of the order of 0.1, Eqs. 74 and 75 are very similar to those for the maximum supersaturation in the constant-pressure decline rate case (Eq. 64). Furthermore, because of the closeness of s_{Dn} to s_{Dm}, we can use the sensitivity analysis we conducted before to assess the dependence of $(P_b-P_n)/P_b$ to the various parameters. Thus, in the region where s_{Dm} is insensitive to Δ, the supersaturation $(P_b-P_n)/P_b$ varies linearly with Π_c. When s_{Dm} is more sensitive with an assumed power-law variation with an exponent 1/4, the supersaturation at the minimum pressure roughly varies as

$$\frac{P_b-P_m}{P_b}\sim\left(\frac{\Pi_4}{\Pi_3}\right)^{1/4}\Pi_c^{2/3}\Pi_2^{-1/12} \tag{76}$$

Such a dependence can be used to guide the matching of the experimental data, as discussed below.

The Rate-Dependent Nucleation Model. We close this section by applying a similar analysis, but now for the rate-dependent nucleation model. We recall the rescaled expression

$$\frac{d\phi_q}{dt_D}=h_1^*\exp\left(-\frac{h_2}{s^2}\right) \tag{77}$$

where $h_1^*=h_1\Pi_1^{-3/2}$. We proceed as before to evaluate the time when the maximum supersaturation is reached. For this, we first use the relation $s\sim t_D$ to obtain

$$\frac{d\phi_q}{ds}\approx h_1^*\exp\left(-\frac{h_2}{s^2}\right) \tag{78}$$

the solution of which is readily found

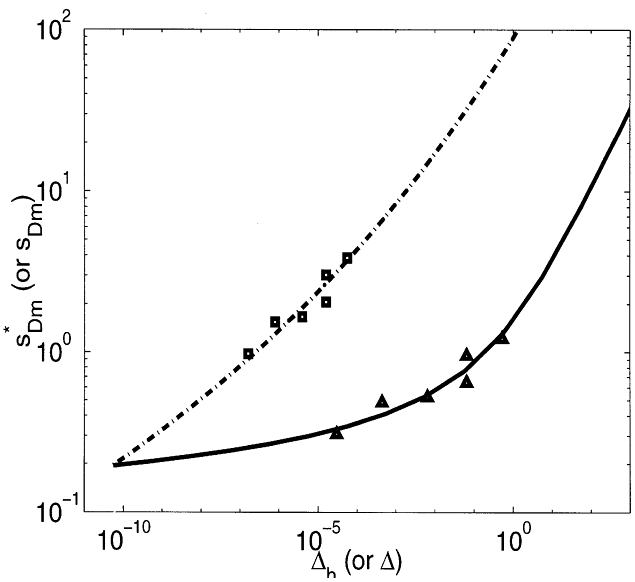

Figure 11. Maximum rescaled supersaturation, s_{Dm}^*, as a function of Δ_h for the simpler model (solid line).

Triangles denote s_{Dm}^* values calculated using experimental data from Scherpenisse et al. (1994). Also plotted are the predictions based on the cavity model (dashed lines for the simpler model, squares denoting s_{Dm} values for the same experiments).

$$\phi_q=h_1^*\left[s\ \exp\left(-\frac{h_2}{s^2}\right)-\sqrt{\pi h_2}\,\mathrm{erfc}\left(\frac{\sqrt{h_2}}{s}\right)\right] \tag{79}$$

The maximum supersaturation occurs when the righthand side of Eq. 52 vanishes, which in this model approximately occurs when the following equation is satisfied

$$s_{Dm}^{*3}\exp\left(-\frac{1}{s_{Dm}^{*2}}\right)-s_{Dm}^{*2}\sqrt{\pi}\ \mathrm{erfc}\left(\frac{1}{s_{Dm}^*}\right)=\Delta_h^{3/2}\Lambda^{-1} \tag{80}$$

Here, we defined the reduced supersaturation $s_D^*=s/\sqrt{h_2}$ and the dimensionless parameter

$$\Delta_h=\Pi_1h_1^{-2/3}h_2^{-1}\Pi_2^{-1/3}$$
$$\left(=\Pi_1^{5/3}\zeta^{-2/3}h_2^{-1}\Pi_2^{-1/3}\ \text{or}\ =\frac{\Pi_4^{5/3}}{\Pi_3}\zeta^{-2/3}h_2^{-1}\Pi_2^{-1/3}\right) \tag{81}$$

For relatively small s_{Dm}^*, the solution of the preceding equation reads

$$\frac{1}{s_{Dm}^{*2}}-5\ \ln\ s_{Dm}^*\approx\ln\ \Lambda-\frac{1}{2}\ \ln\ 3-\ln\ 2-\frac{3}{2}\ \ln\Delta_h \tag{82}$$

A plot of the solution of Eq. 80 is shown in Figure 11. We note features very similar to the cavity nucleation model, namely a region of weak sensitivity at small Δ_h and of stronger sensitivity at higher Δ_h. The rescaled supersaturation for the rate-dependent nucleation model is slightly higher in the region of small Δ_h, but its rate of increase at higher Δ_h is weaker than for the cavity model. Given the dependence of Δ_h on rate, the dependence of the maximum supersaturation could, at first, be considered stronger. For example, for s_{Dm}^* to vary as a power law of the rate with exponent m, it suffices for it to follow a power law with respect to Δ_h with exponent $3m/5$. Interestingly, however, this higher sensitivity is counterbalanced by the lower sensitivity to Δ_h at higher values of Δ_h, compared to the cavity model. For example, if we were to demand $m = 1/4$, then we should consider a range of Δ_h in Figure 11 where the exponent is of the order of 3/20. As shown in the figure, this roughly corresponds to the same range as that of Δ, for the cavity model (Figure 10).

The nucleation fraction at the time of the maximum supersaturation can be estimated as before. We find

$$f_{qf} = s_{Dm}^{*\,-2} h_2^{-1} \left(\frac{\Pi_2}{3}\right)^{-1/2} \Pi_1^{3/2} \Lambda^{-1} \tag{83}$$

As expected, the nucleation rate increases with a decreasing h_2, namely, with smaller values of the interfacial tension γ and the nucleation parameter f. Here the combination $h_1^{1/2} h_2^{3/4}$ plays the role of Π_c. For the same reasons as before, the pressure at the end of nucleation, which is also approximately the minimum pressure, is given by

$$\frac{P_b - P_m}{P_b} \approx \sqrt{h_2}\, s_{Dm}^* \tag{84}$$

In matching experimental data using this model, we would need to infer two parameters, the rate constant K_{het} and the heterogeneous parameter f. This is discussed below.

Working likewise for the case of constant liquid withdrawal rate we find that the previous equations are valid if we replace Π_1 with Π_4/Π_3, and take $\Lambda \equiv \kappa/\Pi_3$.

Gas-cluster growth

The modeling of the growth regime where nucleation has terminated can also be simplified if we consider only one class of clusters. For the case of a constant pressure decline rate we approximate

$$\frac{dC_{D\infty}}{dt_D} \approx -(C_{D\infty} - 1 + t_D) z - C_{D\infty} \Pi_3 \tag{85}$$

and

$$(1 - t_D) \frac{dz^{D_f}}{dt_D} = k_1^{-1} (C_{D\infty} - 1 + t_D) z + z^{D_f} \tag{86}$$

where we introduced the variable

$$z \equiv \phi_{qf} \rho_D \tag{87}$$

and the parameter

$$k_1 = \frac{\phi_{qf}^{1-D_f}}{\Pi_2} \tag{88}$$

The final value of the rescaled nucleation fraction, ϕ_{qf}, as well as the initial values for $C_{D\infty}$ and ρ_D needed for the calculations, are obtained from the previous analysis. Likewise, for the case of constant liquid withdrawl rate, we have similar equations

$$\frac{dC_{D\infty}}{dt_D} \approx -\frac{1}{\Pi_3}(C_{D\infty} - P_{Dl}) z - C_{D\infty} + C_{D\infty} \kappa k_2 \frac{dz^{D_f}}{dt_D} \tag{89}$$

and

$$\Pi_3 P_{Dl} \frac{dz^{D_f}}{dt_D} + z^{D_f} \left(\kappa k_2 \frac{dz^{D_f}}{dt_D} - 1 \right) = k_2^{-1} (C_{D\infty} - P_{Dl}) z \tag{90}$$

along with

$$\frac{dP_{Dl}}{dt_D} \approx \frac{1}{\Pi_3} \left(\kappa k_2 \frac{dz^{D_f}}{dt_D} - 1 \right) \tag{91}$$

and where we defined

$$k_2 = \frac{\phi_{qf}^{1-D_f}}{\Pi_2} \tag{92}$$

To use the simplified growth model, we take initial values for $C_{D\infty}$, ρ_D, P_{Dl}, and ϕ_{qf} corresponding to the time the local minimum pressure is reached. Note that P_{Dl} might be known experimentally, while one can take $C_{D\infty} \approx 1$ without introducing significant error.

Comparison of the full solution with the approximate model is shown in Figure 12. We note a good agreement. In particular, the approximate model captures well the pressure increase, following the minimum, its subsequent leveling, and the gradual decline paralleling the equilibrium curve. The system under consideration has parameters corresponding to the Berea sandstone experiments of Firoozabadi et al. (1992) with $Q = 1.44$ cm^3/day. This system is discussed in further detail in the next section.

Comparison with Experiments

Constant pressure decline rate

The preceding models were subsequently checked against published experimental results. We attempted to match the following quantities and their dependence on parameters, particularly on rate: the final nucleation fraction, the maximum supersaturation, s_{Dm}, the critical gas saturation, S_{gc}, and the evolution of the pressure or saturation as a function of time.

Experimental data for the maximum supersaturation for the case of constant pressure decline rate were reported by Moulu and Longeron (1989) and Scherpenisse et al. (1994). In these experiments, the maximum estimated value for the capillary number was approximately 10^{-8}, which is well within the range of the validity of the model. In addition, the macroscopic capillary number, $Ca_m = Ca(L/\sqrt{k})$, where L is the

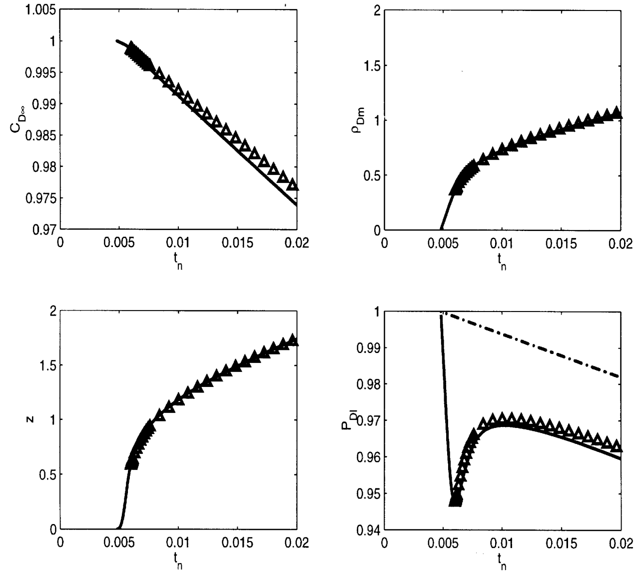

Figure 12. Full numerical results (solid lines) vs. approximate model (denoted by triangles) for the constant liquid withdrawal rate.

Dashed-dotted line in the last panel is the thermodynamic equilibrium curve.

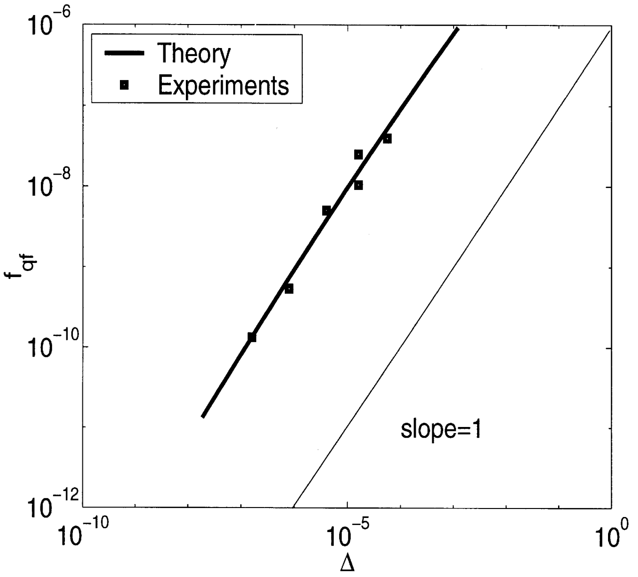

Figure 13. Final nucleation fraction, f_{qf}, as a function of Δ, for a stretched exponential ($n = 0.215$ and $\sigma = 0.045$) cavity-size distribution.

The solid line corresponds to the simpler model, squares denote values calculated using experimental data from Scherpenisse et al. (1994).

length of the core, was of the order of 10^{-3}, indicating negligible viscous pressure gradients. Matching the results requires the use of a window in the s_{Dm} vs. Δ relationship, where a 1/4 power-law is approximately observed. The corresponding windows were identified in Figure 11 both for the rate-dependent nucleation model and the cavity model. The combination Δ contains a number of geometric variables, which are not known *a priori*. The cavity-size distribution is also unknown. We used best estimates for V_s and a range of values for the cavity-size characteristics, to indicate the range of Δ where the various experimental results fall for various size distributions considered. Theory and experiments for the mixture $C1/C5$ in the Berea sandstone experiments by Scherpeniesse et al. (1994) match well, assuming a stretched exponential distribution with values $n = 0.215$ and $\sigma = 0.045$. In these experiments, for r_s^* and r_c^* we used the values suggested by the authors. For the experiments involving the mixture $C1/C3/C10$ in a limestone core, reported by Moulu and Longeron (1989), the corresponding best-fit values were $n = 0.152$ and $\sigma = 0.049$, respectively. These indicate a significantly stretched (long-tailed) cavity-size distribution, with small characteristic sites (see also Table 2 for additional data regarding the experiments).

The predictions of the rate-dependent nucleation model were also tested. Here, the parameters to be estimated include f and the heterogeneous nucleation rate, K_{het}, since

$$\Delta_h \sim K_{\text{het}}^{-2/3} f^{-1} \tag{93}$$

Matching of the experiments of Scherpenisse et al. (1994) required the following parameter values: $f = 2. \times 10^{-4}$ and $K_{\text{het}} = 0.02119\ (\text{cm}^3 \cdot \text{s})^{-1}$ (Figure 11). Correspondingly, for the experiments by Moulu and Longeron (1989) the following best-fit parameter values were found: $f = 3.6 \times 10^{-6}$ and $K_{\text{het}} = 6.45 \times 10^{-6}\ (\text{cm}^3 \cdot \text{s})^{-1}$. Both these sets of values are extreme for the heterogeneous model considered.

Estimates for the final nucleation fraction for the experiments by Scherpenisse et al. (1994) are shown in Figure 13. The final nucleation fraction in the experiments was estimated as suggested by Scherpenisse et al. (1994). Then, f_{qf}

Table 2. Fluid and Porous Medium Properties for Experiments*

Parameter	I	II	III	IV	V
Porous medium	Berea sandstone	St. Maxim limestone	Berea sandstone	Chalk	Quartz sand-pack
Fluid system	C_1/C_5	$C_1/C_3/C_{10}$	C_1/C_{10}	C_1/C_{10}	$C_1/PAO-100$
Length (cm)	~ 15	5	49.04	50.495	60
Diameter (cm)	~ 5	5	3.9116	3.759	n.a.
Porosity %	23.0	29.3	22.3	40.4	38.6
Permeability (m^2)	1.20×10^{-12}	2.08×10^{-13}	5.97×10^{-13}	2.66×10^{-15}	1.10×10^{-12}
Pore volume (cm^3)	n.a.	n.a.	132.24	225.16	487.00
P_b (MPa)	6.0	2.844	7.384	7.627	3.964

*(I) Scherpenisse et al. (1994); (II) Moulu and Longeron (1989); (III), (IV) Firoozabadi et al. (1992); (V) Kumar et al. (2000). (n.a.): not available.

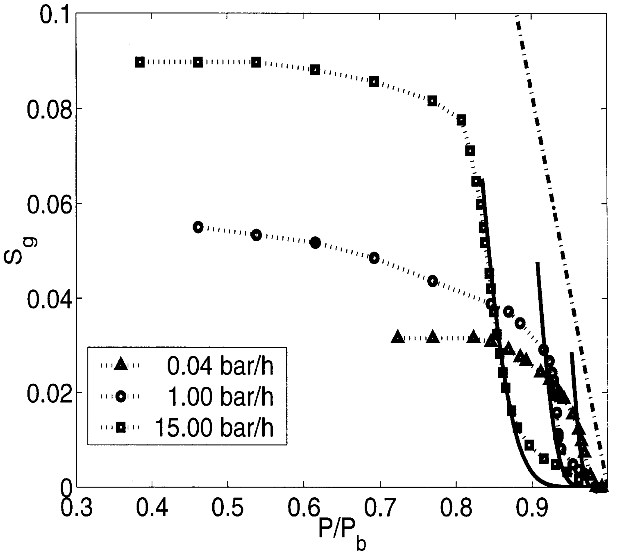

Figure 14. Evolution of the gas saturation as a function of the dimensionless pressure for three depletion rates for the Berea sandstone experiments of Scherpenisse et al. (1994).

Points denote experimental values, solid lines correspond to the full numerical solution, the dashed-dotted line corresponds to the thermodynamic equilibrium curve.

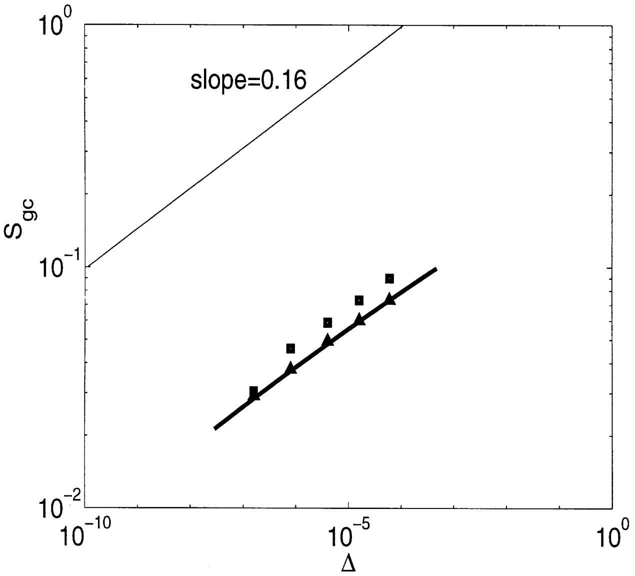

Figure 15. Critical gas saturation, S_{gc}, as a function of Δ, for a stretched exponential ($n = 0.215$ and $\sigma = 0.045$) cavity-size distribution.

The solid line corresponds to the simpler model, triangles denote the full solution, squares denote experimental data (constant pressure decline rate) from Scherpenisse et al. (1994).

was calculated using Eq. 25. As anticipated, f_{qf} is quite small, of the order of 10^{-10}–10^{-7}. The power-law scaling with exponent 1, predicted by the theory in this range, is well supported by the data. Finally, a comparison of the evolution of the gas saturation, S_g, as a function of the dimensionless pressure $P_{Dl} = P/P_b$, using the full solution for the Berea sandstone experiments of Scherpenisse et al. (1994) is presented in Figure 14. Good agreement is observed for the early part of the curve, namely before the gas saturation starts to approach an asymptotic value. The latter stage corresponds to the flow of gas out of the sample, which the present theory does not take into account. The dependence of S_{gc} on f_{qf} was tested against the data of Scherpenisse et al. (1994). Shown in Figure 15 are predictions for both the critical gas saturation as a function of Δ from the simpler model and from the full solution. Although there is a slight tendency for the theory to underestimate the data, we note quite a good agreement. In particular, the power-law scaling with exponent 0.16, predicted by the theory, is well supported by the data.

One of the most interesting effects is that of the pressure decline rate. Quantifying its effect is significant, as one can then control the extent of nucleation, the value of the critical gas saturation, and the time of the onset of bulk gas flow, which for practical purposes signifies the end of the liquid production. An important result of this work has been the derivation of simple algebraic equations (for example, Eqs. 56–59, 80) that relate the critical supersaturation to a combination of dimensionless parameters that involve the rate, given the particular nucleation characteristics of the system. The model developed shows that the effect on the nucleation fraction, and, hence, on the critical gas saturation, is a power law, with an exponent that is equal to 3/2 at low rates, decreases to 1 at higher rates, and ultimately becomes zero at very high rates. The critical supersaturation was predicted to be independent of the rate at small rates, and to be dependent as a weak power law (with an exponent equal to 1/4 or larger) at higher rates. It also can be readily shown that for very large depletion rates, the maximum supersaturation is insensitive to the particular size distribution, scaling as a power law with exponent 3/4. In that limit, the final nucleation fraction is also independent of the rate depletion.

It is interesting that for the experimentally reported rate effect to be matched requires a considerably stretched (long-tailed) cavity-size distribution and small cavity sizes. Equivalently, if the heterogeneous, rate-dependent nucleation model is used, matching the experiments requires that the wettability parameter and the nucleation rate constant have very small values. A long-tailed cavity-size distribution leads to a larger nucleation fraction, provided that the decline rate is not extremely large. Then, more cavity sizes are nucleated at the early stages of the process, as (large) sizes are available for activation even under very small supersaturations. It is possible that this is due to the nucleation of large cavities, exposed at the opening of the core for which a very small supersaturation is needed. Because of the existence of nucleated bubbles early during the process, the maximum supersaturation obtained for a long-tailed distribution is smaller than for a narrow distribution (such as a Rayleigh), when the rates are not too large. Because the rate of depletion becomes very large, the supersaturation eventually becomes the same for all distributions, there is a large window in the rate dependence, where the behavior is like the experimentally reported 1/4 power law. A similar explanation holds for the case of the rate-dependent heterogeneous nucleation model, where a very small value of the wettability parameter favors the nucleation of bubbles even at small supersaturation.

Constant rate of liquid withdrawal

The model was also compared with the experimental results for the case of the constant rate of liquid withdrawal. We matched the local minimum pressure and the related maximum supersaturation, P_n and s_{Dn}, respectively, the critical gas saturation, S_{gc}, and the evolution of pressure as a function of time.

Consider, first, matching the minimum pressure and its rate-dependence. Using the simpler model, this can be done by fitting parameters r_c^*, r_s^* (if not available) and the cavity-size distribution. We first performed this matching for the mixture C1/C10 in the Berea sandstone experiments of Firoozabadi et al. (1992). In these experiments, the estimated values for Ca and Ca_m were 10^{-9} and 10^{-3}, respectively, well within the assumptions of our theory.

Best-fit values $r_s^* = 1.0 \times 10^{-2}$ cm, $r_c^* = 2.0 \times 10^{-3}$ cm, $n = 0.1014$, and $\sigma = 0.0339$ (for a stretched exponential cavity distribution) were found for a good match. The calculated minimum pressure, P_n, using the full solution and the parameters just given are very close to the experiment, as shown in Table 3. Comparison of the evolution of the system pressure as a function of the dimensionless time, $t_n = t_D$, using the full solution, and the Berea experiments of Firoozabadi et al. (1992), is presented in Figure 16. Good agreement is also observed.

A comparison with the chalk experiments of Firoozabadi et al. (1992), for two different reported volumetric flow rates, was also undertaken. Again, $Ca \simeq 10^{-8}$ and $Ca_m \simeq 10^{-2}$ are within the assumptions of our model. Here, the effect of the rate is rather weak, and a Rayleigh distribution was found to be adequate. Based on $r_s^* = 1.0 \times 10^{-4}$ cm, a value of $r_c^* = 1.98 \times 10^{-6}$ cm is needed to match the minimum pressure supersaturation. Figure 17 shows a comparison of the evolution of the liquid pressure as a function of the dimensionless time, $t_n = t_D$, using the full solution. Again good agreement is observed for the pressure evolution, while an excellent match is achieved for the minimum pressures (see Table 3). In both Figures 16 and 17, the predictions from the simpler model closely follow the full solution.

Finally, the theory was tested against the sand-pack experiments of Kumar et al. (2000). In contrast to the preceding, the estimated values for Ca and Ca_m are considerably higher (equal to about 10^{-4} and 10, respectively). This suggests that our model may not adequately capture the physical processes, particularly at later times. Using the best-fit values of $r_s^* = 1.0 \times 10^{-2}$ cm and $r_c^* = 1.0 \times 10^{-3}$ cm, and a stretched exponential cavity size distribution, with parameters $n = 0.3466$ and $\sigma = 0.0134$, leads to a good matching. With these parameters, the ability of the full problem to predict the minimum pressure is good, as can be seen in Table 4. The evolution of the pressure as a function of dimensionless time, t_n, and for different flow rates is shown in Figure 18, based on the simpler growth model. With the exception of the high rate curve, which is not perfectly matched, agreement is good, considering the scatter of the experimental data.

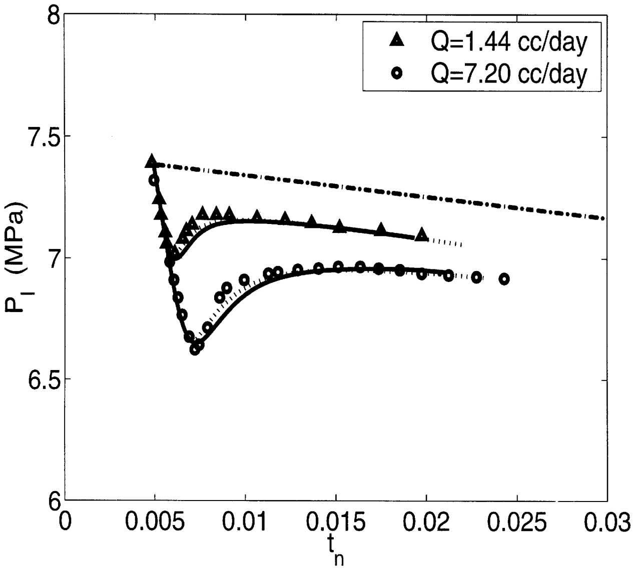

Figure 16. Evolution of pressure as a function of time for the Berea stone experiments of Firoozabadi et al. (1992) for two different withdrawal rates.

Solid lines denote the full solution, dotted lines denote the simpler growth model, the dashed-dotted line denotes the thermodynamic equilibrium curve, symbols denote the experimental results.

A feature that is not well matched in either of these experiments, however, are the values of S_{gc}. The predicted values, using the full solution, are shown in Tables 3 and 4, respectively. The theory systematically overpredicts the experimental data. This disagreement may be due to the different definition of S_{gc}. In this article, the critical gas saturation is defined as the gas saturation when a sample spanning cluster is formed in the absence of gravity or viscous gradients in the system (the presence of which will result in increasing S_{gc}). In the experiments, however, bubbles can be mobilized due to the presence of gradients before the onset of a sample spanning cluster. The disagreement is more profound for the cases of the Berea sandstone or the sand-pack than it is for the chalk. It is also very pronounced in the Kumar et al. (2000) experiments, as explained earlier. This is consistent, since chalk is a tighter porous medium, the capillary and Bond

Table 3. Full Solution vs. Experiments of Firoozabadi et al. (1992)

System	Q (cm^3/d)	P_n^{calc} (MPa)	P_n^{exp} (MPa)	S_{gc}^{calc} (%)	S_{gc}^{exp} (%)	Δ	Π_2	Π_3	Π_4	Π_c
Berea	1.44	6.99664	6.98621	10.8	1.3–2.0	0.30×10^0	0.851×10^4	0.16×10^{-1}	0.62×10^{-5}	0.70×10^{-3}
Berea	7.20	6.64871	6.60689	12.7	1.3–2.0	0.15×10^1	0.851×10^4	0.16×10^{-1}	0.31×10^{-4}	0.70×10^{-3}
Chalk	7.20	7.63703	7.62966	1.6	0.6–1.2	0.38×10^{-7}	0.683×10^6	0.15×10^{-1}	0.46×10^{-8}	0.16×10^0
Chalk	12.96	7.63326	7.62137	1.9	0.6–1.2	0.68×10^{-7}	0.683×10^6	0.15×10^{-1}	0.83×10^{-8}	0.16×10^0

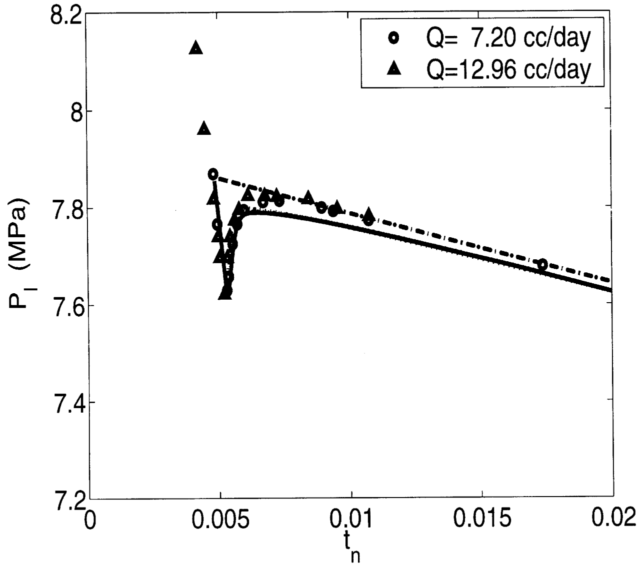

Figure 17. Evolution of pressure as a function of time for the chalk experiments of Firoozabadi et al. (1992) for two different withdrawal rates.

Solid lines (both coincide) denote the full solution, dotted lines denote the simpler growth model, the dashed-dotted line denotes the thermodynamic equilibrium curve, symbols denote the experimental results.

numbers are smaller, and the earlier mobilization of the gas bubbles is less likely.

For completeness, we also estimated the wettability parameter, f, and the heterogeneous nucleation rate, K_{het}, assuming a rate-dependent nucleation model. We found the following for the Berea sandstone experiments (Firoozabadi et al., 1992), $f = 3.305 \times 10^{-5}$ and $K_{\text{het}} = 7.219 \times 10^{-7}$ $(\text{cm}^3 \cdot \text{s})^{-1}$; for the chalk experiments (Firoozabadi et al., 1992), $f = 1.240 \times 10^{-5}$ and $K_{\text{het}} = 2.299 \times 10^{4}$ $(\text{cm}^3 \cdot \text{s})^{-1}$; and for the sand-pack experiments (Kumar et al., 2000), $f = 1.790 \times 10^{-5}$ and $K_{\text{het}} = 1.683 \times 10^{-4}$ $(\text{cm}^3 \cdot \text{s})^{-1}$.

As in the case of a constant pressure decline rate and with the exception of the experiments in chalk, matching of the experimental results with the theory required the use of either stretched, long-tailed cavity-size distributions, or very small wettability parameters in the rate-dependent nucleation model. Such distributions offer the ability to nucleate bubbles even at small supersaturations, and can provide the reported experimental dependence on rate.

Table 4. Full Solution vs. Sand-Pack Experiments of Kumar et al. (2000)*

Q (cm³/d)	P_n^{calc} (MPa)	P_n^{exp} (MPa)	S_{gc}^{calc} (%)	S_{gc}^{exp} (%)	Δ	Π_4
1.92	3.68040	3.80689	9.9	3.0	0.13×10^{0}	0.11×10^{-5}
8.88	3.57088	3.58621	12.7	3.4	0.61×10^{0}	0.52×10^{-5}
72.00	3.31097	3.31034	17.7	4.2	0.49×10^{1}	0.42×10^{-4}
288.00	2.95306	3.05517	22.6	7.0	0.19×10^{2}	0.17×10^{-3}

*For $\Pi_c = 0.655 \times 10^{-3}$; $\Pi_2 = 0.395 \times 10^{3}$; and $\Pi_3 = 0.205 \times 10^{-1}$.

Conclusions

In this article we developed an effective continuum model to describe the nucleation and subsequent growth of a gas phase from a supersaturated, slightly compressible binary liquid in a porous medium, driven by solute diffusion. The evolution of the gas results either from the reduction of the system pressure at a constant rate, or from the withdrawal of the liquid at a constant rate. The model addresses two stages before the onset of bulk gas flow: nucleation and gas-phase growth. We assume negligible gradients due to gravity or viscous forces, so the critical gas saturation, which signals the onset of bulk gas flow, is only a function of the nucleation fraction.

We showed that the important quantities characterizing the process, such as the fraction of pores that host activated sites, the deviation from thermodynamic equilibrium, the maximum supersaturation in the system, and the critical gas saturation, depend crucially on the nucleation characteristics of the medium. We used heterogeneous nucleation models primarily in the form of preexisting gas trapped in hydrophobic cavities, but also in terms of a rate-dependent nucleation, to investigate in detail the nucleation behavior. Using scaling analysis and a simpler analytical model, we showed that the relevant quantities during nucleation can be expressed in terms of a simple combination of dimensionless parameters, which include rate effects, for either type of nucleation model.

The theory predicts that the maximum supersaturation in the system is a weakly increasing function of rate, which in the region of typical experimental parameters, can be approximated as a power law with a small exponent. This function depends sensitively on the probability density function of the nucleation cavity sizes. It also predicts that the final nucle-

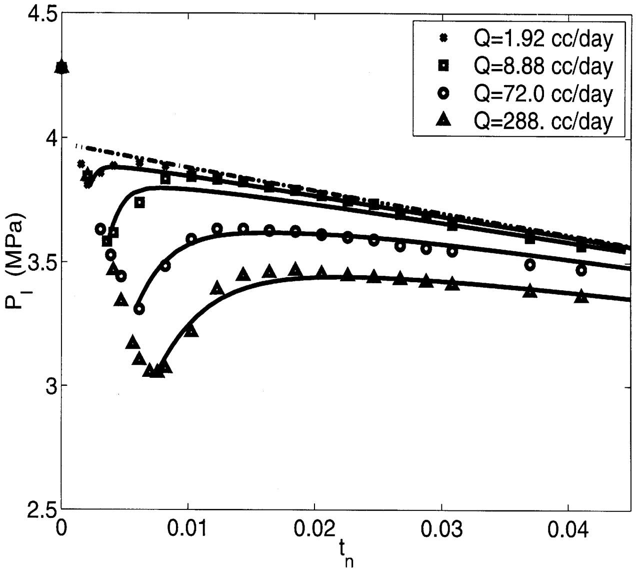

Figure 18. Evolution of pressure as a function of time for the sand-pack experiments of Kumar et al. (2000) for four different withdrawal rates.

Solid lines denote the simpler growth model, the dashed-dotted line denotes the thermodynamic equilibrium curve, symbols denote the experimental results.

ation fraction, and, thus, the critical gas saturation, is a power law of the decline rate (or the withdrawal rate). The theoretical exponents were shown to fit the experimental data, provided a stretched exponential distribution for the cavity size distribution is used.

Acknowledgments

This work was supported by DOE Contract DE-AC26-99BC11521, the contribution of which is gratefully acknowledged.

Literature Cited

Andarcia, L., A. M. Kamp, and P. Vaca, "Heavy Oil Solution Gas Drive in the Venezuelan Orinoco Belt: Laboratory Experiments and Field Simulation," SPE Int. Thermal Operations and Heavy Oil Symp., Margarita Island, Venezuela (2001).

Arora, P., and A. R. Kovscek, "Mechanistic Modeling of Solution-Gas Drive in Viscous Oils," SPE Int. Thermal Operations and Heavy Oil Symp., Margarita Island, Venezuela (2001).

Bora, R., B. B. Maini, and A. Chakma, "Flow Visualization Studies of Solution Gas Drive Process in Heavy Oil Reservoirs With a Glass Micromodel," *SPE Res. Eval. Eng.*, **3**, 224 (2000).

Dominguez, A., S. Bories, and M. Prat, "Gas Cluster Growth by Solute Diffusion in Porous Media. Experiments and Automaton Simulation on Pore Network," *Int. J. Multiphase Flow*, **26**, 1951 (2000).

Doughty, C., and K. Pruess, "A Similarity Solution for Two-Phase Fluid and Heat Flow Near High-Level Nuclear Waste Packages Emplaced in Porous Media," *Int. J. Heat Mass Transfer*, **33**, 1205 (1990).

Du, C., and Y. C. Yortsos, "A Numerical Study of the Critical Gas Saturation in a Porous Medium," *Transp. Porous Media*, **35**, 205 (1999).

Egermann, P., and O. Vizika, "Critical Gas Saturation and Relative Permeability During Depressurization in the Far Field and the Near-Wellbore Region," SPE Annu. Technical Conf. and Exhibition, Dallas, TX (2000).

El Yousfi, A., C. Zarcone, S. Bories, and R. Lenormand, "Mécanismes de Formation d'une Phase Gazeuse par détente d'un liquide en Milieu Poreux," *C. R. Acad. Sci. Paris, Sér. II*, **313**, 1093 (1991).

El Yousfi, A., C. Zarcone, S. Bories, and R. Lenormand, "Physical Mechanisms for Bubble Growth During Solution Gas Drive," SPE Annu. Technical Conf. and Exhibition, San Antonio, TX (1997).

Feder, J., *Fractals*, Plenum, New York (1988).

Firoozabadi, A., and A. Aronson, "Visualization and Measurement of Gas Evolution and Flow of Heavy and Light Oil in Porous Media," *SPE Res. Eval. Eng.*, **2**, 550 (1999).

Firoozabadi, A., and D. Kashchiev, "Pressure and Volume Evolution During Gas Phase Formation in Solution Gas Drive Process," *SPE J.*, **1**, 219 (1996).

Firoozabadi, A., B. Ottesen, and M. Mikkelsen, "Measurements of Supersaturation and Critical Gas Saturation," *SPE Form. Eval.*, 337 (1992).

Hawes, R. I., R. A. Dawe, and R. N. Evans, "The Release of Solution Gas from Waterflood Residual Oil," *SPE J.*, **2**, 379 (1997).

Ho, C. K., and K. S. Udell, "Mass Transfer Limited Drying of Porous Media Containing an Immobile Binary Liquid Mixture," *Int. J. Heat Mass Transfer*, **38**, 339 (1995).

Jones, S. F., G. M. Evans, and K. P. Galvin, "Bubble Nucleation from Gas Cavities—A Review," *Adv. Colloid Interface Sci.*, **80**, 27 (1999).

Kamp, A. M., D. D. Joseph, and R. Bai, "A New Modeling Approach for Heavy Oil Flow in Porous Media," SPE Int. Thermal Operations and Heavy Oil Symp., Margarita Island, Venezuela (2001a).

Kamp, A. M., C. Henry, L. Andarcia, M. Lago, and A. Rodriguez, "Experimental Investigation of Foamy Oil Solution Gas Drive," SPE Int. Thermal Operations and Heavy Oil Symp., Margarita Island, Venezuela (2001b).

Kumar, R., M. Pooladi-Darvish, and T. Okazawa, "An Investigation into Enhanced Recovery Under Solution Gas Drive in Heavy Oil Reservoirs," SPE/DOE Improved Oil Recovery Symp., Tulsa, OK (2000).

Laaksonen, A., V. Talanquer, and D. W. Oxtoby, "Nucleation: Measurements, Theory, and Applications," *Annu. Rev. Phys. Chem.*, **46**, 489 (1995).

Li, X., and Y. C. Yortsos, "Visualization and Simulation of Bubble Growth in Pore Networks," *AIChE J.*, **41**, 214 (1995a).

Li, X., and Y. C. Yortsos, "Theory of Multiple Bubble Growth in Porous Media by Solute Diffusion," *Chem. Eng. Sci.*, **50**, 1247 (1995b).

Mackay, E. J., G. D. Henderson, D. H. Tehrani, and A. Danesh, "The Importance of Interfacial Tension on Fluid Distribution During Depressurization," *SPE Res. Eval. Eng.*, **1**, 408 (1998).

Maini, B., "Foamy Oil Flow in Primary Production of Heavy Oil Under Solution Gas Drive," SPE Annu. Technical Conf. and Exhibition, Houston, TX (1999).

Maini, B., "Foamy Oil Flow in Heavy Oil Production," *J. Can. Pet. Technol.*, **35**(6), 21 (1996).

McDougall, S. R., and K. S. Sorbie, "Estimation of Critical Gas Saturation During Pressure Depletion in Virgin and Water-Flooded Reservoirs," *Pet. Geosci.*, **5**, 229 (1999).

Moulu, J. C., "Solution-Gas Drive: Experiments and Simulation," *J. Pet. Sci. Eng.*, **2**, 379 (1989).

Moulu, J. C., and D. L. Longeron, "Solution-Gas Drive: Experiments and Simulation," *Proc. Eur. Symp. on Improved Oil Recovery*, Budapest, Hungary (1989).

Pooladi-Darvish, M., and A. Firoozabadi, "Solution-Gas Drive in Heavy Oil Reservoirs," *J. Can. Pet. Technol.*, **38**, 54 (1999).

Prats, M., *Thermal Recovery*, SPE Monograph, Dallas, TX (1982).

Press, W. H., S. A. Teukolsky, W. T. Vettering, and B. P. Flannery, *Numerical Recipes*, 2nd ed., Cambridge Univ. Press, New York (1994).

Renard, G., J.-F. Nauroy, Ch. Deruyter, J.-C. Moulu, J.-P. Sarda, and J.-F. Le Romancer, "Production Froide des Huiles Visqueuses," *Oil Gas Sci. Technol.—Rev. IFP*, **55**, 35 (2000).

Satik, C., and Y. C. Yortsos, "A Pore Network Study of Bubble Growth in Porous Media Driven by Heat Transfer," *ASME J. Heat Transfer*, **118**, 455 (1996).

Scherpenisse, W., K. Wit, A. E. Zweers, G. Shoei, and A. van Wolfswinkel, "Predicting Gas Saturation Buildup During Depressurization of a North Sea Oil Reservoir," Eur. Petroleum Conf., London (1994).

Sheng, J. J., B. B. Maini, R. E. Hayes, and W. S. Tortike, "Critical Review of Foamy Oil Flow," *Transp. Porous Media*, **35**, 157 (1999a).

Sheng, J. J., R. E. Hayes, B. B. Maini, and W. S. Tortike, "Modeling Foamy Oil Flow in Porous Media," *Transp. Porous Media*, **35**, 227 (1999b).

Smith, G. E., "Fluid Flow and Sand Production in Heavy-Oil Reservoirs Under Solution-Gas Drive," *SPE Prod. Eng.*, **3**, 169 (1988).

Tang, G.-Q., and A. Firoozabadi, "Gas and Liquid-Phase Relative Permeabilities for Cold Production from Heavy Oil Reservoirs," SPE Annu. Technical Conf. and Exhibition, Houston, TX (1999).

Thome, J. R., *Enhanced Boiling Heat Transfer*, Hemisphere, New York (1990).

Tsimpanogiannis, I. N., PhD Diss., Univ. of Southern California, Los Angeles (2002).

Tsimpanogiannis, I. N., and Y. C. Yortsos, "A Numerical Study of the Critical Gas Saturation in a Porous Medium in the Presence of Gravity Gradients," (2002).

Urgelli, D., M. Durandeau, H. Foucault, and J.-F. Besnier, "Investigation of Foamy Oil Effect from Laboratory Experiments," SPE Int. Thermal Operations and Heavy Oil Symp., Bakersfield, CA (1999).

Wang, X., and K. K. Mohanty, "Critical Condensate Saturation in Porous Media," *J. Colloid Interface Sci.*, **214**, 416 (1999).

Wong, R. C. K., F. Guo, J. S. Weaver, and W. E. Barr, "Heavy Oil Flow Under Solution-Gas Drive: Pressure Depletion Tests," *J. Can. Pet. Technol.*, **38**, 31 (1999).

Yortsos, Y. C., and M. Parlar, "Phase Change in Binary Systems in Porous Media: Application to Solution Gas Drive," SPE Annu. Technical Conf. and Exhibition, San Antonio, TX (1989).

Manuscript received Mar. 8, 2002.